




Advancing regional satellite-based assessment of phytoplankton size structure in a subtropical Bight

Andréa de Lima Oliveira, Natália Rudorff, Shubha Sathyendranath, Fabio Dall Cortivo, Silvana Vianna Rodrigues, Daniela Sudatti, Luciano Felício Fernandes, Frederico Brandini & Milton Kampel


To cite this article: Andréa de Lima Oliveira, Natália Rudorff, Shubha Sathyendranath, Fabio Dall Cortivo, Silvana Vianna Rodrigues, Daniela Sudatti, Luciano Felício Fernandes, Frederico Brandini & Milton Kampel (2025) Advancing regional satellite-based assessment of phytoplankton size structure in a subtropical Bight, International Journal of Remote Sensing, 46:22, 8784-8819, DOI: [10.1080/01431161.2025.2572730](https://doi.org/10.1080/01431161.2025.2572730)

To link to this article: <https://doi.org/10.1080/01431161.2025.2572730>

 View supplementary material 

 Published online: 27 Oct 2025.

 Submit your article to this journal 









 Article views: 127

 View related articles 

 View Crossmark data 



Advancing regional satellite-based assessment of phytoplankton size structure in a subtropical Bight

Andréa de Lima Oliveira ^a, Natália Rudorff ^b, Shubha Sathyendranath ^c,
Fabio Dall Cortivo ^a, Silvana Vianna Rodrigues ^d, Daniela Sudatti ^e,
Luciano Felício Fernandes^f, Frederico Brandini ^g and Milton Kampel ^a

^aEarth Observation and Geoinformatics Division (DIOTG), General Coordination of Earth Science (CGCT), National Institute for Space Research (INPE), São José dos Campos, Brazil; ^bMeteorological Satellites and Sensors Division (DISSM), General Coordination of Earth Science (CGCT), National Institute for Space Research (INPE), Cachoeira Paulista, Brazil; ^cNational Centre for Earth Observation, Plymouth Marine Laboratory, Plymouth, UK; ^dDepartment of Analytical Chemistry, Universidade Federal Fluminense, Niterói, Brazil; ^eDepartment of Marine Biology, Universidade Federal Fluminense, Niterói, Brazil; ^fDepartment of Botany, Universidade Federal Do Paraná, Curitiba, Brazil; ^gInstitute of Oceanography, Universidade de São Paulo, São Paulo, Brazil

ABSTRACT



Phytoplankton underpin marine food webs and carbon cycling, converting dissolved carbon dioxide into organic matter and exporting it to deeper layers. However, these organisms are sensitive to environmental changes that affect their growth and community structure differently, which may be represented by their taxonomic structure or cell size categories. Consequently, there is increasing interest in developing and improving satellite-based models for estimating the abundance of phytoplankton size classes (PSCs) and different taxonomic groups. Satellites can reliably estimate two key properties related to phytoplankton biomass and ocean dynamics: chlorophyll-*a* concentration (Chl_{*a*}), the primary pigment of phytoplankton, and sea surface temperature (SST), which is associated with water masses and often related to nutrient availability. In this study, we tested different approaches and developed regional models to retrieve PSCs from satellite data. The regional models were fitted to the South Brazil Bight (SBB) in the Southwestern Atlantic Ocean. The *in situ* training and validation datasets were obtained from oceanographic cruises conducted in the SBB during 2019–2022. We applied different model parameterisation schemes to compare SST-independent and SST-dependent models with both global and regional fits. The models were applied to both *in situ* data and satellite observations from Ocean and Land Colour Instrument (OLCI) sensors on board Sentinel 3A and 3B satellites, alongside the Multi-scale Ultra-high Resolution (MUR) SST product. The regional SST-dependent approach consistently outperformed alternatives across all size classes, achieving correlation coefficients (*r*) greater than 0.7, bias less than 0.14, and mean


ARTICLE HISTORY

Received 10 June 2025
Accepted 4 October 2025

KEYWORDS

Ocean colour; OLCI Sentinel 3; South Brazil Bight; phytoplankton size classes

CONTACT Andréa de Lima Oliveira  andrea.oliveira@inpe.br  Earth Observation and Geoinformatics Division (DIOTG), General Coordination of Earth Science (CGCT), National Institute for Space Research (INPE), Av. dos Astronautas, 1.758, São José dos Campos, 12227-010, São Paulo, Brazil

 Supplemental data for this article can be accessed online at <https://doi.org/10.1080/01431161.2025.2572730>.

© 2025 Informa UK Limited, trading as Taylor & Francis Group

absolute error (MAE) of less than 0.36. By comparison, the regional SST-independent approach ($\rho > 0.54$, bias < 0.17 , MAE < 0.38) and the global SST-dependent approach ($\rho > 0.59$, bias < 0.11 , and MAE < 0.40) showed weaker performance. These results highlight the importance of regional SST-dependent models for improving PSC estimation accuracy in the SBB and similar regions where SST variability affects nutrient availability, phytoplankton biomass, and community structure.

1. Introduction

Phytoplankton, being at the base of the food web in the pelagic marine ecosystem, serves as the primary link between atmospheric carbon uptake and the biological realm. Consequently, phytoplankton play a pivotal role in biological processes that are critical to the biogeochemical carbon budget. Phytoplankton cell size determines the fate of assimilated carbon: for example, smaller phytoplankton cells remain suspended longer in the upper ocean layer, whereas larger cells sink faster, preferentially transporting the organic carbon in the cells to the deep ocean. A part of the motivation to identify and map phytoplankton size classes (PSCs) or taxonomic groups by satellite remote sensing is to improve the spatial and temporal coverage of observations. Such products are essential for validating biogeochemical models, a task that cannot be fully accomplished by *in situ* sampling techniques alone.

The advent of ocean colour sensors has facilitated the acquisition of quasi-synoptic global distributions of marine phytoplankton, typically represented by the concentration of chlorophyll-*a* (Chl*a*), the major phytoplankton pigment (Jeffrey 1997). For nearly three decades, missions equipped with sensors dedicated to ocean-colour applications have been operating (Groom et al. 2019). These data have proven to be a valuable resource for detecting changes in phytoplankton dynamics in a warming climate (Behrenfeld et al. 2016; Dutkiewicz et al. 2019). Several models have been developed to take satellite products beyond total Chl*a* to estimates of PSCs (Brewin et al. 2010, 2011, 2015; Sun et al. 2023; Turner et al. 2021). Abundance-based models that use Chl*a* to underpin the size partitioning have been extensively used with good results for both global and regional applications (Brewin et al. 2010, 2011, 2015; Sun et al. 2023; Turner et al. 2021). Some of these approaches have incorporated ancillary data such as sea surface temperature (SST) in addition to ocean colour, thereby adding an environmental context to the models (Brewin et al. 2017; Sun et al. 2023). Other types of models exploit the spectral qualities of the ocean-colour signal. Some algorithms are based on spectrally resolved water-leaving radiance (Alvain et al. 2005, 2008; Li et al. 2013; Sun et al. 2025), whereas others are based on the light absorption coefficient (Ciotti and Bricaud 2006; Devred et al. 2011) or back-scatter coefficient (Kostadinov, Siegel, and Maritorena 2010). These approaches will potentially benefit from the utilisation of hyperspectral sensors, such as the Plankton, Aerosol, Cloud, ocean Ecosystem (PACE) satellite launched in 2024, which is equipped with the Ocean Colour Instrument (OCI). A primary objective of the mission is to improve the retrieval of the composition of phytoplankton communities from space (Cetinić et al. 2024). However, alongside advances in retrieval schemes that employ hyperspectral data,

there is also a recognized need to access long-term changes using historical ocean-colour time series from multispectral sensors (e.g. SeaWiFS, MODIS, VIIRS, MERIS, and OLCI, among others). Furthermore, there is a pressing need for further improvements in PSC retrieval in coastal environments are critical, given the optically complex nature and high-frequency dynamics of these waters.

Recent studies have suggested that incorporating SST into abundance-based models could enhance the estimation of PSC, given that a decrease in phytoplankton size is frequently observed alongside an increase in temperature, and vice versa. Models that depend only on Chl a , would not be able to capture such a temperature dependence. In fact, improvements of this kind have been demonstrated using this approach (e.g. Brewin et al. 2017; Sun et al. 2023). Here, we focus on models designed to retrieve the size structure of phytoplankton communities using multispectral ocean-colour data, alongside SST data. The SST incorporation in the model is based on two aspects: the influence of temperature on phytoplankton physiology, such as the maximum of photosynthesis at light saturation conditions and also nutrient uptake rates (López-Urrutia and Morán 2015), and its covariation with nutrient availability (Brewin et al. 2017; Marañón et al. 2012). Typically, relatively colder water masses are richer in nutrients, especially under upwelling conditions. Furthermore, SST is routinely obtained from thermal infrared and microwave sensors and is a well-established, validated, and accurate variable (Minnett et al. 2019), which is available from satellites. As ocean-colour and SST are independent datasets, they are not subject to the same errors and interferences, making SST a robust complement to ocean-colour data for use in PSC models.

There are several global PSC models (Brewin et al. 2010; Devred et al. 2006; Hirata et al. 2008; Sun et al. 2023), which are not generally considered optimal for regional applications (Oliveira et al. 2025). In the global ocean, latitudinal and seasonal differences, such as light limitation in high latitudes during the winter (Arteaga, Pahlow, and Oschlies 2014), and nutrient limitation in tropical and subtropical regions (Arteaga, Pahlow, and Oschlies 2014; Martiny et al. 2013), can influence phytoplankton growth. In addition, shelf and coastal waters may pose additional challenges to the parametrisation of models that are not considered in global models. These include the influence of suspended material and coloured dissolved organic matter in the underwater light field, various sources and processes regulating the intrusion of nutrients up to the surface, and a more diverse phytoplankton community. Consequently, the employment of regionally tuned models may yield more precise outcomes concerning phytoplankton size structure (Turner et al. 2021).

The present study focuses on improving a recently developed regional abundance-based model for a subtropical shelf region (Oliveira et al. 2025) by incorporating SST dependence into the model. Two variants of incorporating SST dependence into regional-tuned model are investigated, and the performance is evaluated against regional SST-independent and global SST-dependent algorithms.

The study area encompasses the continental shelf of the South Brazil Bight, located within the Southwestern Atlantic Ocean. This region is of particular interest due to its dynamic oceanographic processes, including seasonal coastal upwelling and mesoscale eddies and meandering of the Brazil Current (Castro 2014; Silveira et al. 2023). Earlier studies (Oliveira et al. 2025; Oliveira et al. 2021) have suggested that temperature significantly influences PSC in the study region. This study aims to assess whether incorporating SST dependencies can improve PSC retrieval accuracy, evaluating both *in situ* and satellite performance of the models.

2. Methodology

2.1. Study area

The South Brazil Bight (SBB), located in the Southwestern Atlantic Ocean, is bounded to the north by Cabo Frio (23° S) and to the south by Cabo de Santa Marta (28.4° S). The western continental side is bordered by the coastal regions of the following states: Rio de Janeiro (RJ), São Paulo (SP), Paraná (PR), and Santa Catarina (SC), and the eastern offshore side is delineated by the 3000 m isobath (see [Figure 1](#)).

The hydrography structure of the SBB has been extensively documented in previous studies (Castro and Miranda 1998; B. Castro et al. 2006; Emílsson 1961; Miranda 1982; Silveira et al. 2000). According to Silveira et al. (2000) and Mahiques et al. (2004), certain characteristics of the SBB continental shelf structure impact its hydrodynamics and sedimentological patterns. These characteristics include its width along the shelf, which is shorter in the northern portion (Cabo Frio) varying from 50 to 60 km, and wider in the centre portion (off Santos) varying from 200 to 230 km. And the orientation of the coast-line is from E-W direction in the northern portion and NE-SW direction further south.

Three main water masses are placed over the continental shelf, slope, and oceanic domains. The Tropical Water (TW) is a warm ($> 20^{\circ}\text{C}$), saline (> 36), and nutrient-poor water mass that dominates the surface ocean layer and is transported southward along

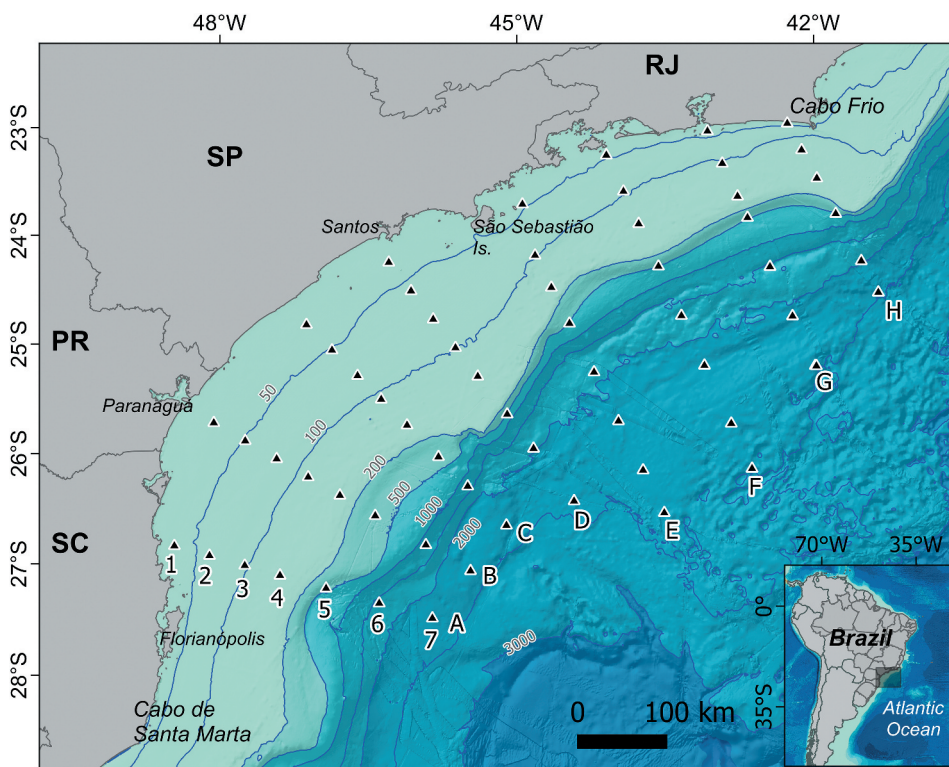


Figure 1. The South Brazil Bight in the Southwestern Atlantic Ocean. Sampling stations represented by black triangles and bathymetry in meters (GEBCO Compilation Group 2024).

the continental slope by the Brazil Current (Castro et al. 2006; Emílsson 1961), also extending over the continental shelf near the shelf break (Silveira et al. 2000). The South Atlantic Central Water (SACW) underlies the TW and is characterised by lower salinity (34.6–36), lower temperatures ($< 20^{\circ}\text{C}$), and high nutrient concentrations, with seasonal upwelling on the inner- and mid-shelf driven by persistent north-easterly winds that enhance vertical transport during the austral spring and summer (B. M. Castro and Miranda 1998; Cerda and Castro 2014; Brandini, Tura, and Santos 2018). The Coastal Water (CW) occupies the nearshore surface layer formed by the mixing of TW, SACW, and low salinity freshwater from river discharge (Castro and Miranda 1998). A fourth water mass, the La Plata Plume Water (PPW) is characterised by low salinity (< 33.5) and low temperature ($> 10^{\circ}\text{C}$), in addition to variable nutrient concentrations (Möller et al. 2008), and exerts a notable influence within the southernmost region of the SBB, particularly in the vicinity of São Sebastião Island. The influence is indicated by the Subtropical Shelf Front (SSF) which transports the PPW northwards (Brandini, Tura, and Santos 2018).

The water column is subject to the influence of atmospheric processes, including the passage of cold fronts during the austral winter and spring months. These events result in a shift in prevailing winds from a northeast to a southeast direction, thereby enhancing water column mixing (de Castro Filho et al. 2015). Mesoscale oceanic eddies along the meandering Brazil Current front drive the SACW onto the shelf as the current flows southwestward along the shelf break (Campos, Velhote, and Silveira 2000; Silveira et al. 2000), while in the winter, there is the northward advection of the PPW into the SBB (Brandini, Tura, and Santos 2018; Piola et al. 2000). Collectively, these processes influence the hydrographic conditions of the SBB region, thereby affecting variability in phytoplankton assemblages (Oliveira et al. 2021).

Several studies have examined phytoplankton distribution patterns and their relationships with environmental drivers in the SBB (Alves Junior et al. 2015; Bergo et al. 2017; Ribeiro et al. 2016; Tenenbaum et al. 2004; Villac, Cabral-Noronha, and Pinto 2008). Though these studies are somewhat geographically limited and seasonally fragmented, there are clear cross-shelf differences in phytoplankton composition, characterised by differences in the relative importance of phytoplankton groups such as diatoms, dinoflagellates, cyanobacteria, and picoeukaryotes (Brandini 2018). With respect to pico-sized phytoplankton, a numerical dominance of cyanobacteria is commonly observed at the surface of the mid- and outer-shelf regions, and is influenced by the proximity of oligotrophic, warm waters from the Brazil Current, leading to low nutrient concentrations (Alves Junior et al. 2015; Bergo et al. 2017; Ribeiro et al. 2016). Within the euphotic zone at the mid and outer-shelf regions, the genus *Synechococcus* belonging to the cyanobacteria group, and flagellated picoeukaryotes exhibit higher abundances. However, at the shelf break, this community is replaced by cells belonging to the genus *Prochlorococcus* of the same order (Synechococcales) as *Synechococcus*, under the extremely oligotrophic conditions of the water column. Conversely, nearshore areas display a distinct phytoplankton composition, where the background of pico-sized phytoplankton is supplemented by a remarkably diverse coastal phytoplankton assemblage of larger organisms, particularly in upwelling areas and those influenced by estuarine inputs (Brandini et al. 1997; Fernandes and Brandini 2004; Valentin, Andre, and Jacob 1987). The dominant taxonomic groups in these coastal regions are diatoms and flagellated cells of nano- and micro-sized

phytoplankton (Fernandes and Brandini 2004; Tenenbaum et al. 2004; Villac, Cabral-Noronha, and Pinto 2008). The distribution of these diatom-rich waters along the inner shelf is primarily influenced by tidal and geostrophic currents (Brandini 2018).

2.2. *In situ* sampling and measurements

The *in situ* dataset was obtained from oceanographic cruises carried out as part of the Regional Environmental Characterisation of the Santos Basin (PCR-BS) project (Moreira et al. 2023). The sampling grid followed the isobaths of eight transects perpendicular to the coastline, from shallow (continental shelf) to deep waters (continental slope and plateau). The number of stations in each transect ranged from 6 to 8, depending on the extent of the continental shelf, yielding a total of 60 stations that were sampled twice to encompass the austral winter/early-spring (8 August 2019 to 27 October 2019) and summer/early-autumn (14 December 2021 to 29 March 2022) seasons, with a total of 120 surface (≤ 5 m) water samples, to support satellite-based analysis.

Vertical profiles of water-column temperature and salinity, as well as the maximum Chl a concentration and mixed-layer depths were obtained with a Sea-Bird Electronics 9plus CTD profiler equipped with a pressure, conductivity, and chlorophyll- a fluorescence sensor, among others, deployed at each station.

Surface seawater samples were collected directly from the Niskin bottles and filtered onto Whatman GF/F filters using a 60 ml polypropylene syringe coupled to a 25 mm filter holder for laboratory analyses of dissolved inorganic nutrients. Prior to each station, the syringe was washed with Milli-Q ultrapure water and rinsed thrice with sample water. Seawater samples were collected in 10 ml sterilized Falcon bottles for nitrate, nitrite, phosphate and silicate analyses, and in 25 ml amber glass bottles previously rinsed with 10% HCl for ammonium samples. All samples were collected in triplicate and stored at -20°C until laboratory analysis. At the onshore laboratory, the concentrations of nitrate, nitrite, phosphate, and silicate were determined using an AA3-Seal autoanalyzer, while ammonium was determined using a Hitachi U-1100 spectrophotometer (Grasshoff, Kremling, and Ehrhardt 1999).

For the analysis of phytoplankton pigment, 5 L of seawater were filtered using 25 mm diameter GF/F membrane filters (Millipore, MA). The filters were then stored in liquid nitrogen until laboratory analysis. The concentrations of primary and secondary pigments were obtained using the High Performance Liquid Chromatography (HPLC) method as described in Sanz et al. (2015), with quality control as described in Aiken et al. (2009).

Duplicate subsamples for the analysis of the absorption coefficient of coloured dissolved organic matter (CDOM) were filtered by gravity directly from Niskin/Go-Flow bottles using a Whatman Polycap Aqueous Solution filter device with a pore size of $0.2\ \mu\text{m}$. These subsamples were stored in pre-combusted glass bottles wrapped in aluminium foil and kept refrigerated (4°C) until further laboratory analysis (Mannino et al. 2019). The CDOM absorption coefficient was determined by spectrophotometric absorbance measurements of the filtered CDOM samples at room temperature in a $0.1\ \text{m}$ optical path quartz cell in an onshore laboratory.

The absorption coefficient of particulate matter was measured by filtering up to 2 L of water samples on board in duplicate using 25 mm Whatman GF/F ($0.7\ \mu\text{m}$ nominal pore size) filters, with the time of filtration not exceeding 40 min. The filters were stored in

liquid nitrogen until laboratory analysis. The absorption coefficient of particulate matter was determined onshore using the transmittance-reflectance method (Tassan 2002) using a Shimadzu UV-2450 dual-beam spectrophotometer equipped with an integration sphere. For the absorption coefficient of detritus, a sodium hypochlorite solution with around 0.1% of active Cl (NaClO) was added to the filter after the measurement of the absorption of particulate matter (described above). This solution bleaches the phytoplankton pigments, and after 15 min, it is gently washed from the filter, which is measured again for the absorption coefficient of detritus (Tassan and Ferrari 1995, 2002). The absorption coefficient of phytoplankton is obtained by subtracting the absorption coefficient of detritus from the absorption coefficient of the particulate matter (Tassan and Ferrari 1995, 2002). The absorption coefficients of CDOM, particulate matter, detritus and phytoplankton were analysed using the same spectrophotometer. For further details on measurements, stations, and analysis, please refer to Moreira et al. (2023).

2.3. Satellite data

For the satellite application, Sentinel-3A and –3B OLCI images, with a nominal spatial resolution of 300 m and daily revisits, were downloaded for the sampling days of the validation dataset from <<https://search.earthdata.nasa.gov/search>.>. The images were processed using NASA's SeaDAS software version 8.1, from L1 to L2, through the Ocean Colour (OC) suite. The Chla algorithm is a mixed version of OC4 (O'Reilly and Werdell 2019) and CI (colour index) (Hu, Lee, and Franz 2012) as described by J. Werdell et al. (2023). When Sentinel-3A and –3B Ocean and Land Colour Instrument (OLCI) images were both available matching the sampling date and location, the image closer to the local time of sampling was selected. *In situ* data were matched with the processed satellite images using a window of 3×3 pixels centred on the sampling locations. The matchup was considered valid if the windows contained a minimum of five valid pixels and a coefficient of variance no greater than 20% (Stock and Subramaniam 2020). For the valid matchups, the median value was used.

For models requiring SST, we used the Group for High Resolution Sea Surface Temperature (GHRSSST) Multi-scale Ultra-high Resolution (MUR) Level 4 daily data with a 0.011° spatial resolution grid (JPL MUR MEaSUREs Project 2015). The MUR SST product was utilized for the present work, instead of the Sentinel-3 Sea and Land Surface Temperature Radiometer (SLSTR) SST, because it corresponds to the foundation depth (~ 10 m), which is more representative of the first optical depth. The SST data were resampled to match the spatial resolution of the OLCI images (i.e. 300 m).

2.4. In situ data analysis

2.4.1. Canonical correspondence analysis

A multivariate Canonical Correspondence Analysis (CCA) (Ter Braak and Verdonschot 1995) was used to identify the environmental variables that have important relationships with PSCs, to help explain what triggers their variability and succession, and to identify environmental variables that could be used to improve PSC models in the study region. CCA was applied using the R package 'vegan'. A detailed description of abbreviations and symbols is available in Table A1.

2.4.2. Diagnostic pigment analysis

Prior to the diagnostic pigment analysis (DPA), the quality of the pigment concentrations was controlled using the criteria described by Aiken et al. (2009). Chl *a* concentrations in the picoplankton (< 2 µm), nanoplankton (2–20 µm), and microplankton (> 20 µm) were then estimated following the DPA method described in Uitz et al. (2006) and the updates proposed by Brewin et al. (2010) and Devred et al. (2011).

The weighted sum of the seven diagnostic pigments (C_w) should be equivalent to the value of the total chlorophyll-*a* concentration (TChl *a*), and is obtained following Equation (1):

$$C_w = \sum_{i=1}^7 W_i P_i \quad (1)$$

where W_i is the weight of the i_{th} pigment, and P_i is the concentration of the i_{th} pigment. The seven diagnostic pigments are $i = \{\text{fucoxanthin, peridinin, 19'-hexanoyloxyfucoxanthin, 19'-butanoyloxyfucoxanthin, alloxanthin, total chlorophyll-*b*, and zeaxanthin}\}$. The weights used were $i = \{1.41, 1.41, 1.27, 0.35, 0.60, 1.01, \text{ and } 0.86\}$, respectively (Uitz et al. 2006). TChl *a* is the sum of the following pigments that are separated in the HPLC analysis: monovinyl chlorophyll-*a*, divinyl- chlorophyll-*a*, chlorophyllide-*a*, chlorophyll-*a* allomers and epimers.

The fractions for pico (F_p), nano (F_n), and microplankton (F_m) were estimated following Brewin et al. (2015) using C_w (Equations 2-4):

$$F_p = \begin{cases} \frac{(-12.5C+1)W_3P_3}{C_w} + \frac{\sum_{i=6}^7 W_i P_i}{C_w} & \text{if } TChl\ a \leq 0.08\ mg\ m^{-3} \\ \frac{\sum_{i=6}^7 W_i P_i}{C_w} & \text{if } TChl\ a > 0.08\ mg\ m^{-3}, \end{cases} \quad (2)$$

$$F_n = \begin{cases} \frac{12.5W_3P_3}{C_w} + \frac{\sum_{i=4}^5 W_i P_i + W_1 P_{1,n}}{C_w} & \text{if } TChl\ a \leq 0.08\ mg\ m^{-3} \\ \frac{\sum_{i=3}^5 W_i P_i + W_1 P_{1,n}}{C_w} & \text{if } TChl\ a > 0.08\ mg\ m^{-3}, \end{cases} \quad (3)$$

and

$$F_m = \frac{\sum_{i=1}^2 W_i P_i - W_1 P_{1,n}}{C_w} \quad (4)$$

To account for the fucoxanthin present in nanoplankton, a part of the contribution of this pigment was assigned to the nanoplankton fraction, $P_{1,n}$ which was calculated as follows (Equation 5):

$$P_{1,n} = 10^{q_1 \log_{10}(P_3) + q_2 \log_{10}(P_4)}, \quad (5)$$

where P_3 and P_4 refer to 19'-hexanoyloxyfucoxanthin and 19'-butanoyloxyfucoxanthin, and q_1 and q_2 refer to the coefficients estimated by Devred et al. (2011) for the NOMAD dataset (Werdell and Bailey 2005), 0.531 and 0.708, respectively. The corresponding concentrations of C_p , C_n , and C_m were then obtained multiplying by TChl *a* by the respective F_p , F_n , F_m .

2.4.3. Development of the PSC models

To parameterise the PSC models, a subset of samples (80%, $N = 96$) was randomly selected for the training dataset. We investigated the performance of four different model parameterisations for estimating PSC, all based on adaptations of the abundance-based (AB) approach of Brewin et al. (2010):

- (A) the ‘classical’ AB approach regionally fitted (SST-independent),
- (B) the AB approach using an SST-threshold to regionally fit the model in two steps (above/below the SST-threshold),
- (C) an SST-dependent AB approach, regionally fitted using a ‘SST moving window’, following Sun et al. (2023) (regional SST-dependent), and
- (D) same as (C) but using the global fit of Sun et al. (2023) (global SST-dependent).

As mentioned, the models are adaptations of the AB approach of Brewin et al. (2010) using regional fits (A) and incorporating SST dependencies (B and C) (only D corresponds to a global fit, SST-dependent approach). The global AB approach (Brewin et al. 2010) was not included in the comparison because it has already been demonstrated that the regional fit works better for the SBB (Oliveira et al. 2025). Further details of the model parameterisations are given below.

Model A – Abundance-based regional fit (SST-independent). This model is based on the abundance-based (AB) approach using the TChla as input and exponential functions (Equations 6–9) to estimate the fractionated Chla corresponding to picoplankton (C_p), pico- and nanoplankton ($C_{p,n}$) and microplankton (C_m) size classes, as described in Brewin et al. (2010), according to Equations (6–9):

$$C_p = C_p^{max} \left[1 - \exp \left(- \frac{D_p}{C_p^{max}} TChla \right) \right] \quad (6)$$

$$C_{p,n} = C_{p,n}^{max} \left[1 - \exp \left(- \frac{D_{p,n}}{C_{p,n}^{max}} TChla \right) \right] \quad (7)$$

$$C_n = C_{p,n} - C_p \quad (8)$$

and

$$C_m = TChla - C_{p,n} \quad (9)$$

The regionally adjusted model parameters for picoplankton, and combined pico- and nanoplankton, respectively, are the maximum asymptotic chlorophyll-*a* concentration (C_p^{max} , $C_{p,n}^{max}$), and the slope D_p and $D_{p,n}$, which also determine the size-partitioned Chla as TChla tends to zero for picoplankton (Figure 2). The fitting of these parameters is achieved using the TChla, equivalent to the weighted sum of the diagnostic pigments (C_w) (Equation 1), and the fractionated chlorophyll-*a* concentrations C_p , C_n , C_m and $C_{p,n}$ (Equations 1–5). The fitting was done on log-transformed data. In this model the parameters C_p^{max} , $C_{p,n}^{max}$, D_p and $D_{p,n}$ are constant, i.e., do not change with SST.

Model B – Abundance-based regional fit with an SST-threshold. In this model, we adopted an SST threshold and fitted Equations 6–9 to the *in situ* training dataset, after

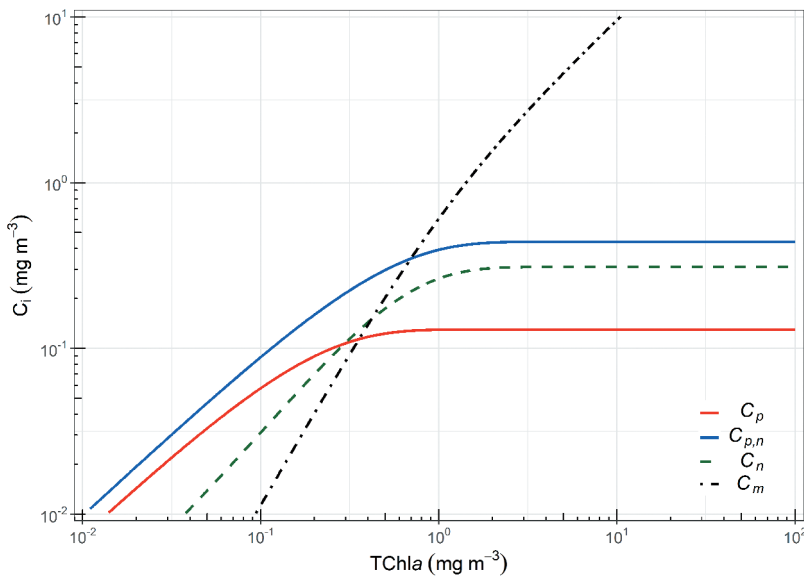


Figure 2. Relationship between TChla and C_i (sized fraction chlorophyll), each curve represents the relationship for TChla and C_i for each PSCs (pico, nano, pico+nano, and micro) showing the adjusted curves for model A, as defined by the initial slope ($D_p, D_{p,n}$) and asymptotic chlorophyll ($C_p^{max}, C_{p,n}^{max}$) values, determined by the Equations 6-9.

partitioning the data into two parts: below and above the SST-threshold. Even for the limited range of SST in the study region (17.6–27.8 °C), a variation of the parameters was observed with a change in SST, when the parameters were fitted to running bins of 30 samples, and the results plotted against the mean SST values for those bins (Figure 3). The observed variation was then used to determine the SST threshold: The parameter D_p presented values lower than 0.6 for temperatures below 24.5°C, with a clear increase above this temperature. $D_{p,n}$ presented values greater than 0.9 for the entire SST range. But there were still some temperature-dependent changes, with two plateaus at the extremities of the SST range and a valley in the centre (at around 23.8 °C) (Figure 3(a)). The maximum asymptotic chlorophyll concentrations showed a rough Gaussian-like curve for C_p^{max} and $C_{p,n}^{max}$, with peak also at 23.8°C (Figure 3(b)). Based on these variations of the parameters with temperature, we selected 23.8°C, which was also the median temperature of the training dataset, as the thermal threshold and fitted the model separately for stations with temperatures below/above it.

Model C – Abundance-based SST-dependent regional fit. There have been previous models that were developed for PSC estimation that included SST. Different strategies have been proposed to account for the effect of SST on PSC. Brewin et al. (2017) used logistic functions for four SST-dependent parameters, such that the model required a set of 16 parameters overall. Then, Sun et al. (2023) developed a 17-parameter model, which will be described in more detail in the next section. Here, we fit a 15-parameter model for the SBB region. The starting point for this model is the same as for Model B, in which we used a bin size of 30 and applied a sliding running bin to estimate the parameters $C_{p,n}^{max}, C_p^{max}, D_{p,n}$ and D_p (Figure 3).

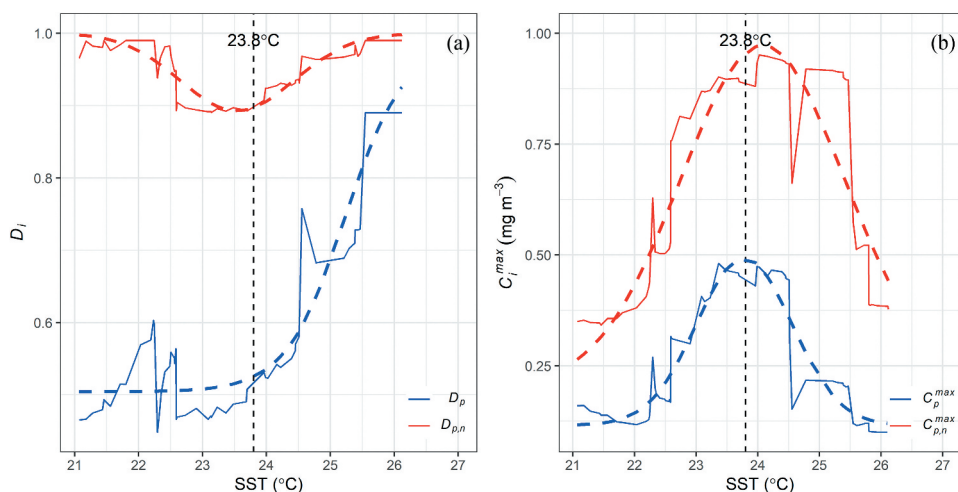


Figure 3. The curves represent the values fitted to running bins of 30 samples and the mean SST values for those bins. The black dashed line denotes the median temperature of the training dataset. The coloured dashed curves represent the fitted values of the parameters (D_i and C_i^{max} , where i is the corresponding size class pico or pico and nanoplankton) for model C.

However, instead of using the results for identifying a temperature threshold for partitioning the data into two groups, in Model C we fit a continuous function to capture the temperature dependence.

In contrast to the curves observed by Sun et al. (2023), the $C_{p,n}^{max}$ and C_p^{max} curves in this study tended to follow a Gaussian curve (see Equations 10 and 11 and Figure 3(b)). This deviation from the Sun et al. (2023) curves may be attributed to the narrower range of SST in the region. The relationship between D_p and temperature could be explained using a logistic relationship (Equation 13 and Figure 3(a)), as in Brewin et al. (2017). Nevertheless, in contrast to the curve described in Brewin et al. (2017) and Sun et al. (2023), the fitted $D_{p,n}$ values in this study did not follow a logistic curve (Figure 4(a)), with values greater than 0.9. Hence, an inverted Gaussian curve with a fixed upper limit was used to fit the training dataset for this equation (Equation 12). The relationships between the parameters and the SST observed in Figure 3 are represented by Equations (10-13):

$$C_{p,n}^{max} = K_d \exp \left[- \left(\frac{SST - K_b}{K_c} \right)^2 \right] + K_d \quad (10)$$

$$C_p^{max} = L_d \exp \left[- \left(\frac{SST - L_b}{L_c} \right)^2 \right] + L_d \quad (11)$$

$$D_{p,n} = -M_d \exp \left[- \left(\frac{SST - M_b}{M_c} \right)^2 \right] + 1 \quad (12)$$

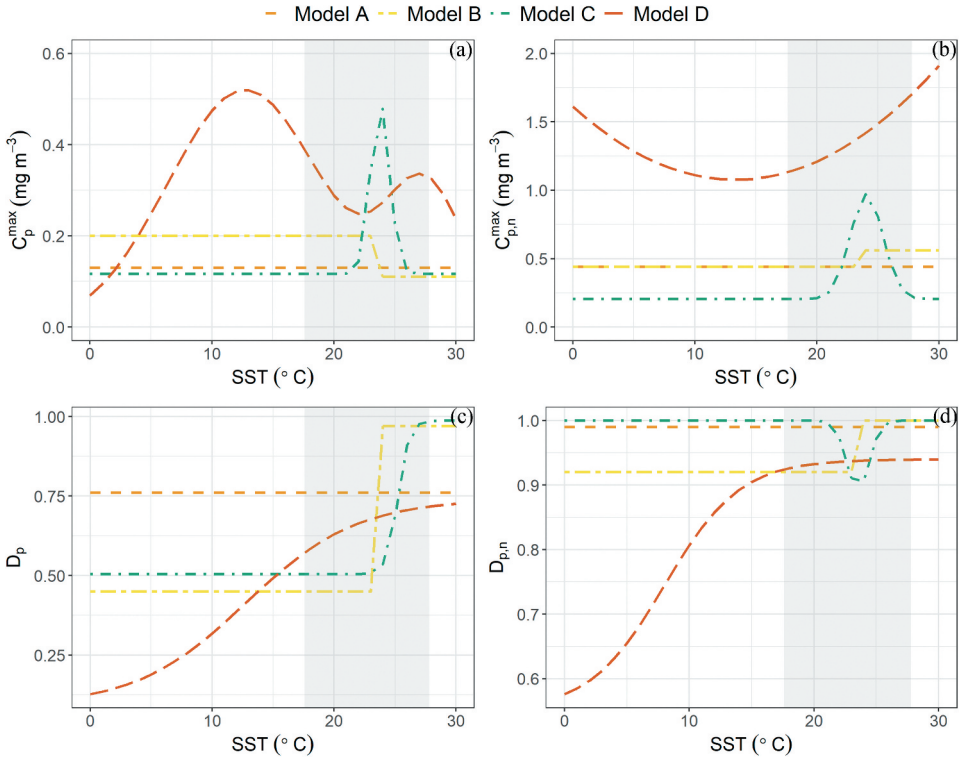


Figure 4. Relationships between SST and the parameters: (a) C_p^{\max} , (b) $C_{p,n}^{\max}$, (c) D_p , and (d) $D_{p,n}$, for models a to D. The grey box in the plots represents the SST range of the SBB in-situ data.

$$D_p = \frac{O_a}{1 + \exp[-O_b(SST - O_c)]} + O_d \quad (13)$$

where the parameter K_a is the height of the peak of $C_{p,n}^{\max}$, K_b is the corresponding SST, K_c is the width of the curve, and K_d is the lower limit for $C_{p,n}^{\max}$ (Equation 10). Equation 11 is also a Gaussian with parameters L_i ($i = a, b, c, d$), as described above (for the K_i parameters). Equation 12 (for $D_{p,n}$), on the other hand, is an inverted Gaussian. Therefore, M_a is the depth of the trough for the minimum $D_{p,n}$, and M_b is the corresponding SST. In this case, the upper bound for $D_{p,n}$ is set to one, as values greater than one would be physically unrealistic. For D_p , O_a and O_d are the upper and lower bounds (see Figure 3(a)) of D_p , and O_c is the midpoint of the slope between D_p and SST (see Equation 13).

Model D – Abundance-based SST-dependent global fit. For comparison, we applied the Sun et al. (2023) model with globally fitted SST-dependent parameters, which were determined following the same approach as that described above. The authors employed a much larger database including samples from the global oceans collected across a broad range of latitudes and used significantly larger bin sizes (ranging from 3,000 to 10,000 samples, with increments of 1,000). For the running fit of each bin, the bin was slid from low to high temperature in increments of one sample, with the equations being fitted each time. The range of temperatures in the work of Sun et al. (2023) was considerably broader for their global dataset than that observed for the SBB in the present

study, and ranged from -1.8°C to 32.15°C , with a mean value of 14.47°C . The authors developed a model with 17 parameters by adopting a two-term Gaussian function for C_p^{max} (Equation 14, Figure 4(a), Model D) and a quadratic polynomial function for estimating $C_{p,n}^{max}$ (Equation.15, Figure 4(b), Model D), while keeping the logistic functions for $D_{p,n}$ and D_p (Equations 16 and 17, Figure 4(c,d), Model D). Figure 4 shows the relationship between SST and the model parameters such as Figure 3, but in this case for all models (A-D) and a global SST range for comparison.

$$C_{p,n}^{max} = U_a SST^2 + U_b SST + U_c \quad (14)$$

$$C_p^{max} = V_a \exp \left[- \left(\frac{SST - V_b}{V_c} \right)^2 \right] + V_d \exp \left[- \left(\frac{SST - V_e}{V_f} \right)^2 \right] \quad (15)$$

$$D_{p,n} = \frac{J_a}{1 + \exp[-J_b(SST - J_c)]} + J_d \quad (16)$$

$$D_p = \frac{O_a}{1 + \exp[-O_b(SST - O_c)]} + O_d \quad (17)$$

2.4.4. Validation exercise: application to in situ and satellite data

An independent, randomly selected, subset of in-situ samples (20%, $N = 24$), namely the validation (testing) dataset, was used to evaluate the performance of each model, using Chla and SST as model inputs and comparing the results of the fractions and size-fractionated Chla with the *in situ* DPA PSC data.

The PSC models were also applied to the satellite data, and the results compared with the *in situ* DPA size classes, and the performance metrics were calculated, as outlined in the next section.

2.4.5. Performance metrics and best algorithm selection

The performance metrics chosen to evaluate the PSC models were Pearson's correlation coefficient (ρ), bias (δ), root mean square error (RMSE, ε), mean absolute error (MAE, ψ), and slope (Equations 18-22):

$$\rho = \frac{\sum_{i=1}^n (x_i - \bar{x})(y_i - \bar{y})}{\sqrt{\sum_{i=1}^n (x_i - \bar{x})^2} \sqrt{\sum_{i=1}^n (y_i - \bar{y})^2}} \quad (18)$$

$$\delta = \left(\frac{\sum_{i=1}^n \log_{10}(M_i) - \log_{10}(O_i)}{n} \right) \quad (19)$$

$$\varepsilon = \sqrt{\frac{\sum_{i=1}^n (\log_{10}(M_i) - \log_{10}(O_i))^2}{n}} \quad (20)$$

$$\psi = \frac{\sum_{i=1}^n |\log_{10}(M_i) - \log_{10}(O_i)|}{n} \quad (21)$$

$$\log_{10}(M) = \text{Slope} \cdot \log_{10}(O) + a \quad (22)$$

where M_i and O_i are the modelled and observed values, respectively.

In addition, a visual two-dimensional radar chart was used to help select the best performance model. The performance metrics were normalised (Equations 23-27)

$$\delta_{norm}(j) = \frac{\delta(j)}{\max(\delta(j), j = 1, k)} \quad (23)$$

$$\varepsilon_{norm}(j) = \frac{\varepsilon(j)}{\max(\varepsilon(j), j = 1, k)} \quad (24)$$

$$\psi_{norm}(j) = \frac{\psi(j)}{\max(\psi(j), j = 1, k)} \quad (25)$$

$$\text{Slope}_{norm}(j) = \frac{|1 - \text{Slope}(j)|}{\max(|1 - \text{Slope}(j)|, j = 1, k)} \quad (26)$$

$$\rho_{norm}^2(j) = \frac{\min(\rho^2(j), j = 1, k)}{\rho^2(j)} \quad (27)$$

where j represents each PSC model for the comparison and the subscribed 'norm' indicates the normalised metrics. The results were then plotted on radar charts. The determination coefficient (ρ^2) was used (instead of ρ) to avoid negative values. The radar chart areas were then calculated, and the chart with the lowest area indicated the best performance model. This method provides an effective way to visually and quantitatively identify the best performances considering multiple metrics. However, it should be interpreted with caution, since it can exaggerate small metric differences. The polar coordinates were calculated considering the number of vertices, and then the sine and cosine of the angles were multiplied by the values of the set of normalised performance metrics for each PSC model, finally obtaining the polygon area. The final Equation (28) is shown below:

$$\begin{aligned} \text{Area} = \frac{1}{2} \left| \sum_{i=1}^n ((r_i \cos(\theta_i))(r_{i+1} \sin(\theta_{i+1})) - (r_i \sin(\theta_i))(r_{i+1} \cos(\theta_{i+1}))) \right. \\ \left. + (r_n \cos(\theta_n))(r_1 \sin(\theta_1)) - (r_n \sin(\theta_n))(r_1 \cos(\theta_1)) \right| \end{aligned} \quad (28)$$

where r_i are the normalised performance metrics, θ_i are the corresponding polar coordinate angles, considering a polygon with n vertices (a sequence of equal interval angles up to 2π).

The complete workflow of the various processing steps leading to the best model selection is shown in [Figure 5](#).

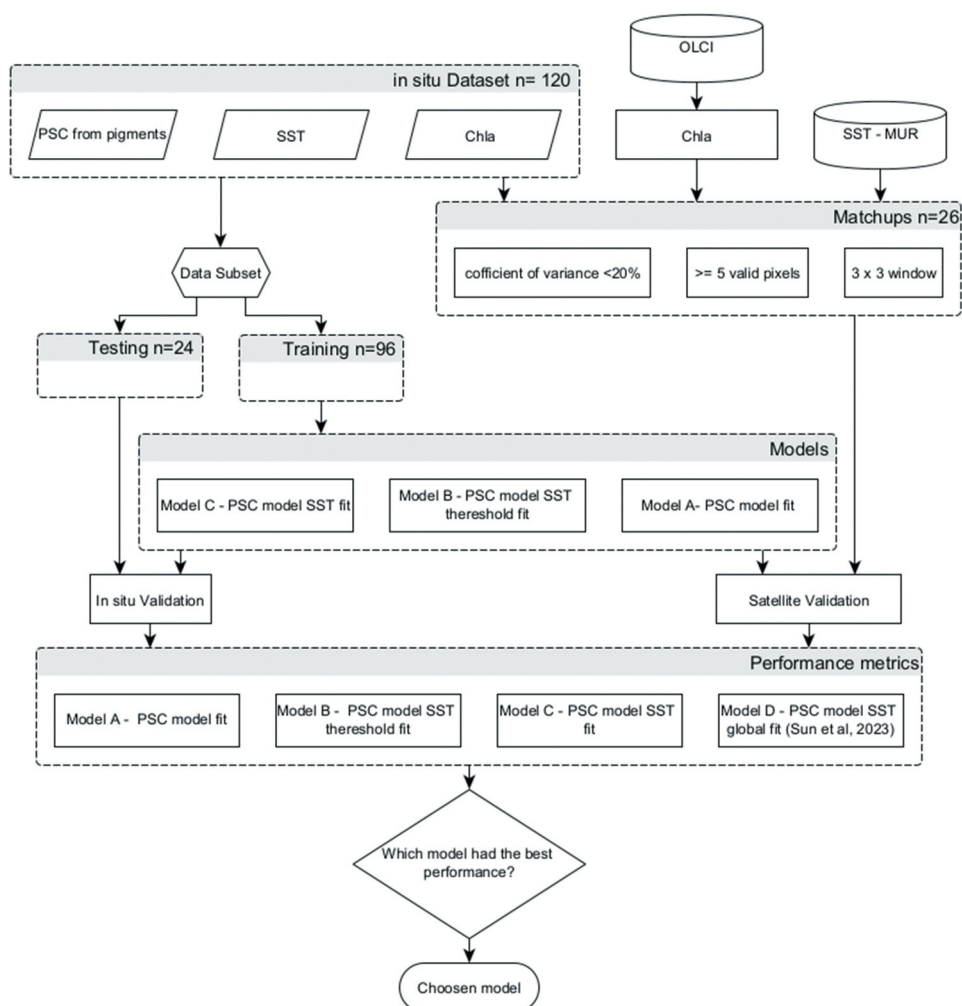


Figure 5. PSC model selection workflow, indicating the in-situ data subsets of the validation/testing and model training; satellite data acquisition and matchups for the application and evaluation of the PSC models and the selection of the best-performing model.

2.5. Spatial-temporal PSC variability in the SBB

Finally, the best-selected model was applied to analyse the spatio-temporal variability of PSCs in the study region (SBB) using OLCI ocean colour and MUR SST products. To maximize the surface coverage, 8-day composites (1 km) were used and selected to represent two contrasting seasons during the *in situ* survey periods: austral winter and summer. These seasons are characterised by distinct water masses and oceanographic processes; summer is dominated by TW, with occasional upwelling events in Cabo Frio, whereas winter is dominated by SSF, with cold waters from the south, as described in the study area section.

3. Results

3.1. Variability in the environmental properties of the SBB

Considering the limited spatial extent of the study region (Figure 1), the SBB exhibited marked environmental variability (Table 1), primarily influenced by terrigenous inputs and seasonal hydrographic dynamics, such as spring-summer coastal upwelling Cerda and Castro (2014). TChla ranged from 0.06 to 2.38 mg m⁻³, with a mean of 0.27 mg m⁻³. SST varied from 17.67°C to 27.86°C, with a mean of 23.39°C, while salinity ranged from 32.6 to 37.3, with a mean of 35.9.

The first CCA component explained more than 95% of the total variability (Figure 6). The results show a strong positive relationship of C_m (microplankton) with TChla, silicate, phosphate, a_{ph} , and a_p , and a negative relationship with SST. Conversely, a positive relationship of picoplankton concentration (C_p) was found between SST, depth of maximum chlorophyll fluorescence (DCM), salinity, and local depth, while negatively related to TChla. The observed positive relationship between nanoplankton concentration (C_n) and the mixed-layer depth (MLD) should be interpreted with caution, since the sampling area extends over different depth ranges, and MLD variability is strongly linked to both local depth (including freshwater influence on the shelf) and seasonality (e.g., deeper MLD during the winter). Despite weaker associations of C_n with TChla and SST, its distribution more closely resembled that of C_p , showing negative relationships with TChla and positive with SST. This pattern supports the grouping of these two size fractions in the PSC models. Overall, these results reinforce the inclusion of SST as a key variable in PSC models for the SBB, considering its strong linkage with nutrients, Chla and PSC, consistent with findings from other continental shelf systems (Turner et al. 2021).

Table 1. Statistics of measured water properties. The units of each variable are in parentheses. Minimum (min), maximum (max), mean and standard deviation are shown. TChla, sea surface temperature (SST), mixed-layer depth (MLD), depth of the chlorophyll-*a* maximum (DCM), ammonia (NH₄), nitrite (NO₂⁻), nitrate (NO₃⁻), silicate (SiO₄⁻⁴), absorption coefficient for non-algal particulate matter (a_{nap}), absorption coefficient for phytoplankton (a_{ph}), absorption coefficient for coloured dissolved organic matter (a_{cdom}), and absorption coefficient for particulate matter (a_p).

Variable	Min	Max	Mean	Standard deviation
TChla (mg m ⁻³)	0.06	2.38	0.26	0.30
SST (°C)	17.67	27.86	23.39	2.54
Salinity	32.66	37.31	35.88	1.22
MLD (m)	3	182	34	40
Depth (m)	30	2450	926.84	956.42
DCM (m)	3	130	62.67	34.45
NH ₃ (μM)	0.02	1.16	0.27	0.29
NO ₂ ⁻ (μM)	<0.01	0.46	0.04	0.05
NO ₃ ⁻ (μM)	0.01	6.47	0.23	0.701
SiO ₄ ⁴⁻ (μM)	0.08	11.18	2.29	2.43
PO ₄ ³⁻ (μM)	<0.01	0.68	0.21	0.12
$a_{nap}(443)(m^{-1})$	<0.001	0.073	0.003	0.008
$a_{ph}(443)(m^{-1})$	0.003	0.070	0.012	0.009
$a_{cdom}(443)(m^{-1})$	<0.001	0.238	0.039	0.047
$a_p(443)(m^{-1})$	0.003	0.104	0.014	0.015

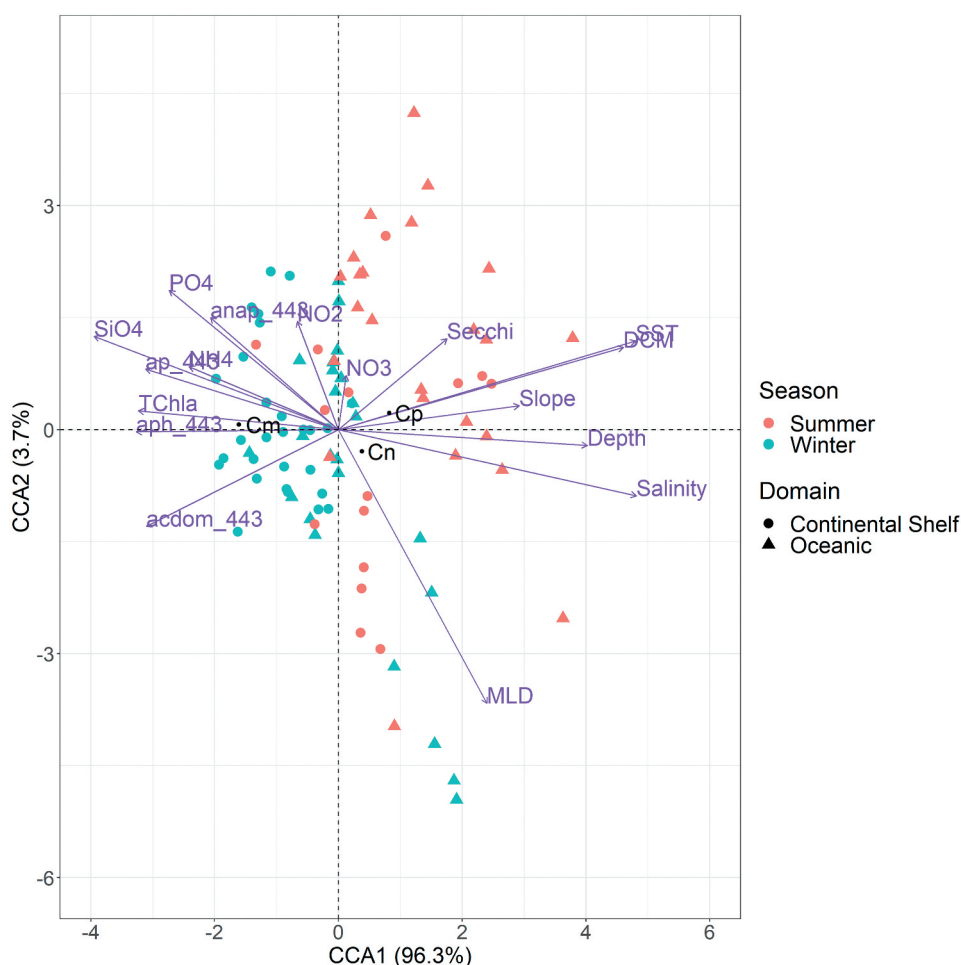


Figure 6. Canonical correspondence analysis biplot. Purple arrows refer to the environmental variables, black dots and black text to phytoplankton size classes, triangles to oceanic stations (> 200 m depth) and circles to continental shelf stations (< 200 m depth). Pink and green represent the summer and winter campaigns, respectively.

3.2. Parameterisations of the PSC models

The values of the parameters of the PSC models obtained for the SBB compared with other studies showed similarities (Table 2). Model A, the regional reparameterisation of the classical AB approach (Brewin et al. 2010), showed similar picoplankton parameters (C_p^{max} and D_p) compared with other studies (Brewin et al. 2011, 2017; Sun et al. 2023), while the pico- and nanoplankton parameters, mainly $C_{p,n}^{max}$, were lower, 0.44 mg m^{-3} in this study and $> 0.77 \text{ mg m}^{-3}$ in the other studies (Table 2).

Model B is also similar to that of Brewin et al. (2017) but using an SST threshold and regionally fitting the parameters in a two-step framework (above/below the threshold). For Model C, compared with Model D, the main difference is the number of parameters; Model C has 15 parameters, while Model D has 17 parameters. The other difference is the

Table 2. Parameter (par) values for models a (SST-independent), B (SST-threshold), C_i^{max} and D_i (SST-dependent), and comparative studies.

SST-independent					SST-threshold				SST-dependent			
Par	Model A	Brewin et al. (2011)	Brewin et al. (2015)	Sun et al. (2023)	Model B (this study) $\leq 23.8^\circ\text{C}$	Model B (this study) $> 23.8^\circ\text{C}$	Brewin et al. (2017) $< 15^\circ\text{C}$	Brewin et al. (2017) $\geq 15^\circ\text{C}$	Par	Model C (this study)	Par	Model D (Sun et al. 2023)
$C_{p,n}^{max}$	0.44	0.78	0.77	0.95	0.44	0.56	1.83	0.86	K_a	0.769	U_a	0.003
									K_b	24.08	U_b	−0.08
									K_c	1.886	U_c	1.61
									K_d	0.204		
C_p^{max}	0.13	0.15	0.13	0.17	0.20	0.11	0.31	0.13	L_a	0.377	V_a	0.52
									L_b	23.78	V_b	12.71
									L_c	−1.092	V_c	8.95
									L_d	0.116	V_d	0.30
											V_e	27.52
											V_f	4.61
$D_{p,n}$	0.99	0.89	0.94	0.87	0.92	1	0.60	0.93	M_a	0.107	J_a	0.39
									M_b	23.54	J_b	0.33
									M_c	1.259	J_c	8.02
											J_d	0.55
D_p	0.76	0.75	0.80	0.67	0.45	0.97	0.26	0.74	O_a	0.483	O_a	0.65
									O_b	2.164	O_b	0.22
									O_c	25.23	O_c	12.79
									O_d	0.504	O_d	0.09

magnitude of the parameters, considering that some of them are related to the temperature range of the training datasets, as illustrated in [Figure 4](#) and related equations.

3.3. In situ PSC application and validation

The independent *in situ* validation dataset ($n = 24$) was used to evaluate the performance of the four PSC models. All models performed reasonably well in estimating the size-fractionated chlorophyll-*a* concentrations ([Figure 7](#)), with ρ values above 0.54, 0.69, 0.68, and 0.69 for C_p , $C_{p,n}$, C_n , and C_m , respectively. For the pico size class, the best results were observed for the regional SST-dependent Model C. The weakest performance was observed for the regional SST-independent Model A, followed by the global SST-dependent Model D. For the pico-nano size class, the best performance was obtained for the regional SST threshold Model B, and for the micro size class, the best performance was for Model C ([Figure 7](#)). According to the radar chart areas, Models B and C, with area values of 1.75 and 1.76, respectively, performed best (since smaller areas indicate better overall performance) ([Figure 9](#) and [Table 4](#)).

Some outliers with high uncertainties for any of the fractioned Chl*a* of the three size classes (> 0.8 absolute error) were highlighted in red in [Figure 7](#). We investigated potential factors that might be responsible for these outliers. The sample highlighted with a red circle is correspondent to a station near the shelf break (D5) sampled during the summer, in which C_m from the PSC models was underestimated in relation to the DPA, while C_n and consequently $C_{p,n}$ were overestimated (absolute error > 0.8) ([Figure 7c, g, k, o](#)). The opposite happened for the samples highlighted with red squares and diamonds, which presented a high overestimation of C_m (absolute error > 0.8) and a minor underestimation of $C_{p,n}$ for the PSC models in comparison with DPA. The red

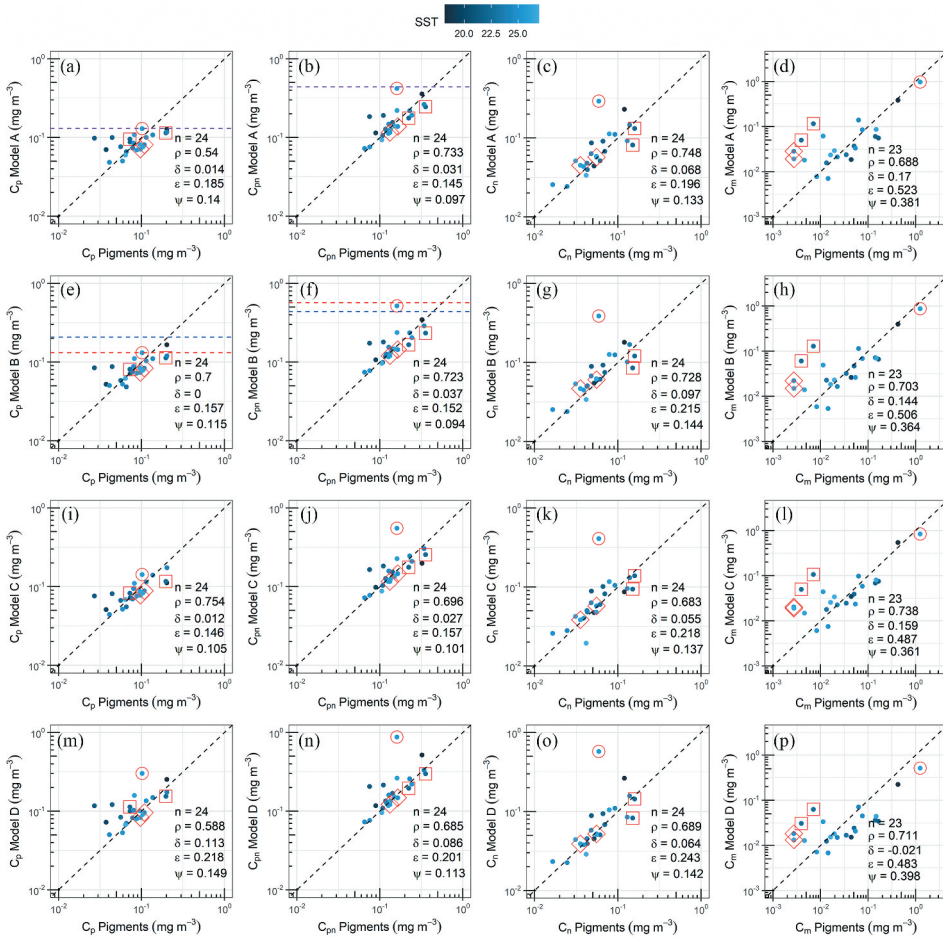


Figure 7. Independent validation of the PSC models applied to the *in situ* dataset, comparing the size-fractionated chlorophyll-*a* concentrations derived from the diagnostic pigment analysis (indicated in the x-axis by 'pigments') and from the respective PSC models: Model a (SST-independent model) (a–d); model B (SST-threshold model) (e–h); model C (15-parameter SST-dependent model) (i–l); model D (17-parameter SST-dependent model (global parameters)) (m–p). The dashed purple line corresponds to the C_p^{max} and $C_{p,n}^{max}$ in a and b. The dashed blue line is the C_p^{max} and $C_{p,n}^{max}$ for SST < 23.8°C and the dashed red line is the C_p^{max} and $C_{p,n}^{max}$ for SST ≥ 23.8°C in figures e and f. The dashed black line in all figures is the 1:1 reference line. Here, n is the number of observations, ρ is the correlation coefficient, δ is the bias, ϵ is the root mean square error, and ψ is the mean absolute error. Red shapes indicate the outliers discussed in the text, the circle is station D5 sampled in summer, the squares are stations E7 and C7 sampled in winter, and the red diamonds are stations B3 and E2 sampled during summer.

squares represent stations sampled at deep waters during the winter (E7 and C7), while the red diamonds represent stations sampled at the inner shelf during the summer (B3 and E2).

When the results are plotted for the relative proportions (fractions) of Chl *a* in each class (Figure 8), the distributions of the data points are different from those for the concentrations (as shown in Figure 7). The statistical metrics also change correspondingly (Table 3).

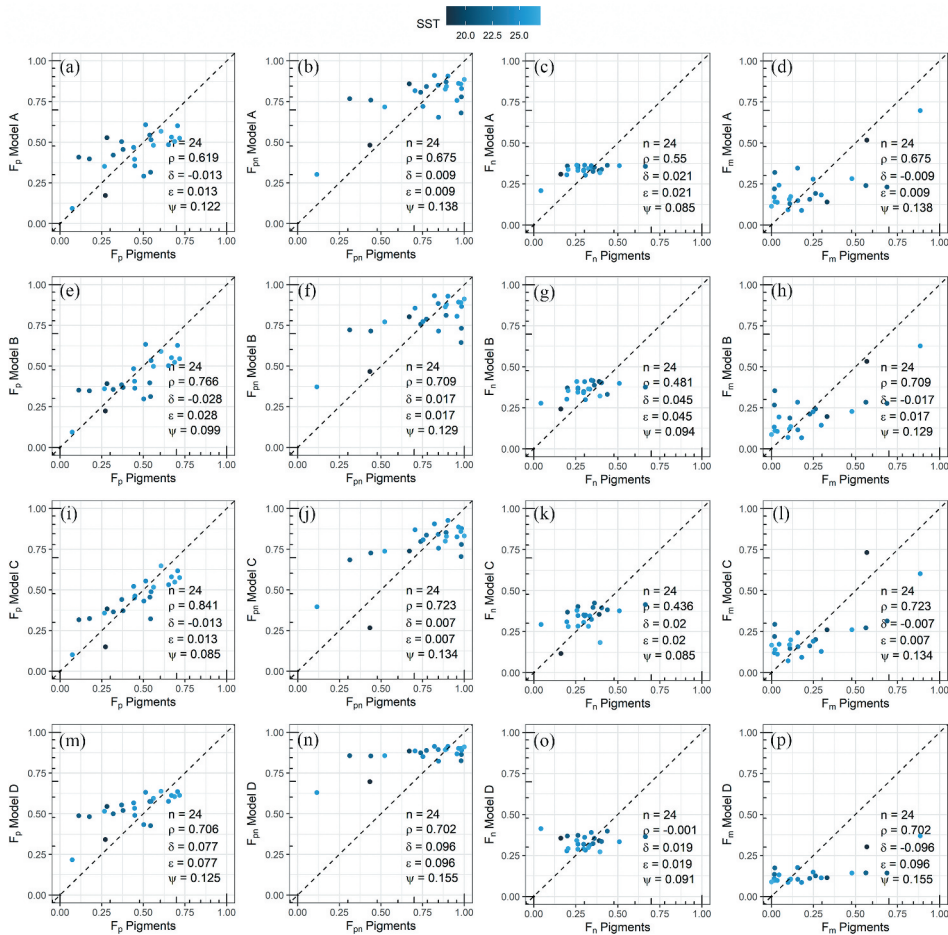


Figure 8. Independent validation of the PSC models applied to the *in situ* dataset, comparing the size fractions derived from diagnostic pigment analysis (indicated in the x axis by 'pigments') and modelled size fractions derived from: Model a (the SST-independent model) (a–d); model B (SST-threshold model) (e–h); model C (15-parameter SST-dependent model) (i–l); and model D (17-parameter SST-dependent model (global parameters)) (m–p). The dashed black line in all the figures is the 1:1 reference line. n is the number of observations, ρ is the correlation coefficient, δ is the bias, ϵ is the root mean square error, and ψ is the mean absolute error.

However, the overall performance was still the best for models B and C, as in the case for the fractionated chlorophyll concentrations (Figure 9 and Table 1).

3.4. Satellite PSC application and validation

When the PSC models were implemented on OLCI ocean colour data (processed with a combination of OC4 and CI chlorophyll algorithms) and MUR SST data, and compared with *in situ* data, the results showed a reasonable performance for all size classes, with ρ values > 0.48, 0.67, 0.68, and 0.73 for C_p , $C_{p,n}$, C_n , and C_m , respectively (Figure 10). Poorer performance was consistently observed for the pico-size class for all models. Model B showed the best overall

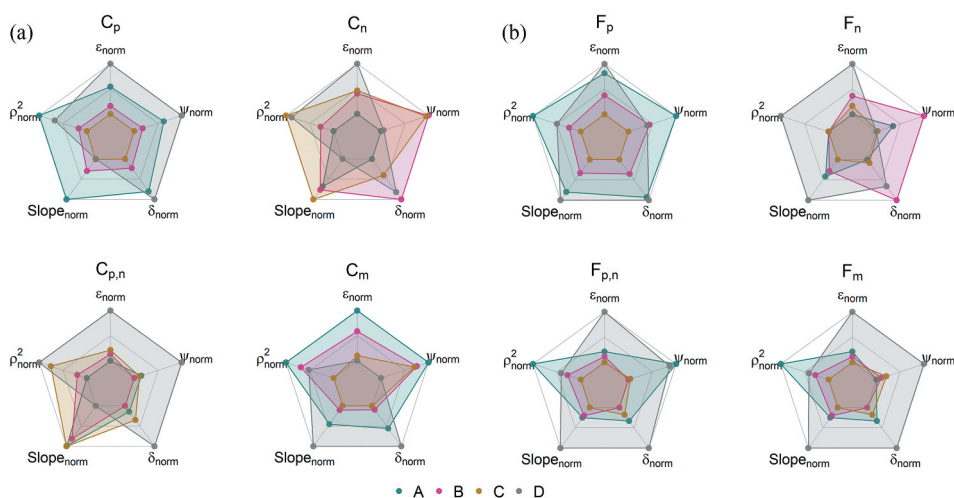


Figure 9. Radar charts of the performance metrics of each model (A–D) (a) for the fractionated Chl *a* of each size class (C_p , C_n , and C_m) and (b) the correspondent fractions (F_p , F_n , and F_m) when compared with the *in situ* validation data.

Table 3. Radar charts areas for the *in situ* PSC validation. Rows in bold indicate the best performance models, with the smallest mean area.

Model	C_p	$C_{p,n}$	C_n	C_m	Mean
Model A	2.06	1.75	1.76	2.26	1.96
Model B	1.21	1.68	2.04	2.07	1.75
Model C	0.98	1.91	2.23	1.93	1.76
Model D	1.96	1.89	1.74	2.08	1.92
Model	F_p	$F_{p,n}$	F_n	F_m	Mean
Model A	2.23	1.87	1.08	1.75	1.73
Model B	1.36	1.63	1.29	1.62	1.47
Model C	0.95	1.55	0.99	1.55	1.26
Model D	1.96	2.29	2.14	2.31	2.17

Table 4. The calculated areas of the radar charts for the satellite validation. Rows in bold indicate the best performance models, with the smallest mean area.

Model	C_p	$C_{p,n}$	C_n	C_m	Mean
Model A	1.98	1.62	1.9	2.09	1.90
Model B	1.7	1.56	1.22	1.65	1.53
Model C	1.95	1.76	1.3	1.64	1.66
Model D	1.96	1.69	1.8	2.32	1.94
Model	F_p	$F_{p,n}$	F_n	F_m	Mean
Model A	2.03	1.59	1.33	1.36	1.58
Model B	1.15	1.4	1.03	1.55	1.28
Model C	1.33	1.21	1.19	1.39	1.28
Model D	2.27	2.31	2.38	2.38	2.34

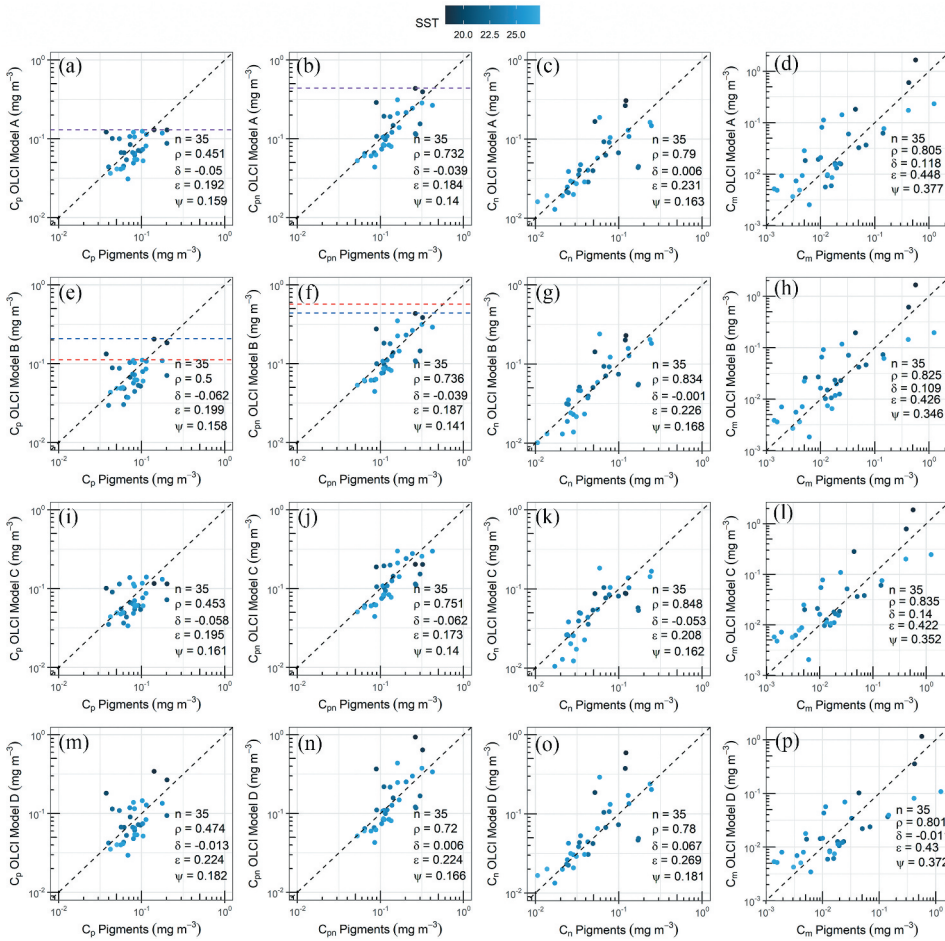


Figure 10. Satellite validation between *in situ* derived diagnostic pigment analysis (indicated in the x axis by 'pigments') and satellite-modelled size-fractionated chlorophyll-1063 " $=0">a$ " concentrations derived from: model a (SST-independent model) (a–d); model B (SST-threshold model) (e–h); model C (15-parameter SST-dependent model) (i–l); and model D (17-parameter SST-dependent model (global parameters)) (m–p). The dashed purple line is C_p^{max} and $C_{p,n}^{max}$ in a and b. The dashed blue line is C_p^{max} and $C_{p,n}^{max}$ for SST < 23.8°C and the dashed red line is C_p^{max} and $C_{p,n}^{max}$ for SST ≥ 23.8°C in e and f. The dashed black line in all the figures is the 1:1 reference line. n is the number of observations, ρ is the correlation coefficient, δ is the bias, ϵ is the root mean square error, and ψ is the mean absolute error.

performance for all size classes when considering the radar chart area for the fractionated Chla concentrations (C_p , $C_{p,n}$, C_n , and C_m), although it performed similarly to Model C for the estimated size fractions (Figure 10–12 and Table 2). Accordingly, both *in situ* and satellite-based validations identified Model B and C as the best performing models for the study region. Validation of the OLCI-derived Chla product (Sentinel-3A and 3B) showed a strong agreement with *in situ* observations (Figure 13), with a correlation coefficient of 0.86, log-transformed bias of –0.05, RMSE of 0.193, and MAE of 0.142. These results suggest that the main uncertainties of the PSC models are not associated with the input satellite Chla product.

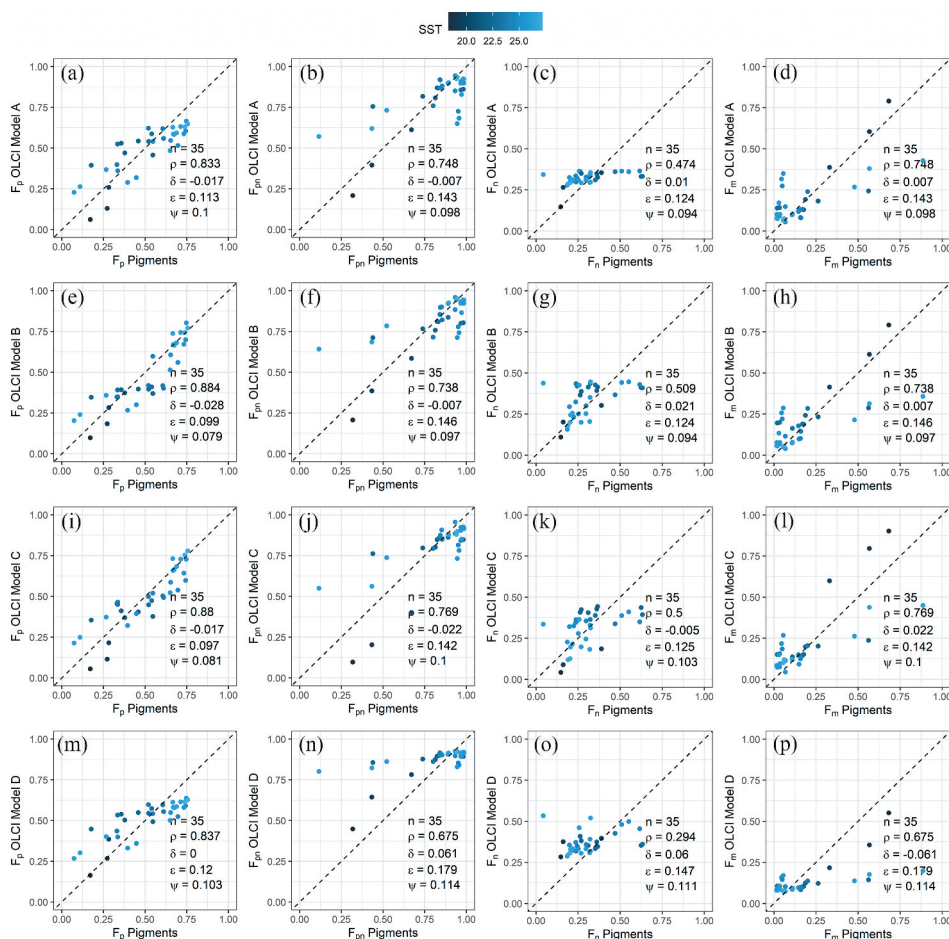


Figure 11. Satellite validation between *in situ* derived diagnostic pigment analysis (indicated in the x-axis by 'pigments') and satellite-modelled size-fractionated fractions of chlorophyll-*a* concentrations derived from: model a (SST-independent model) (a–d); model B (SST-threshold model) (e–h); model C (15-parameter SST-dependent model) (i–l); and model D (17-parameter SST-dependent model (global parameters)) (m–p). n is the number of observations, ρ is the correlation coefficient, δ is the bias, ϵ is the root mean square error, and ψ is the mean absolute error.

The performance of the size fractions was poorer for Model D compared to models B and C (Figure 11, 12). The nano-sized fraction had the poorest results for all models, with correlation coefficients ≤ 0.5 .

3.5. Spatio-temporal variability of PSC in the SBB

Since the overall results of the PSC models were reasonable, we applied Model C (regional SST-dependent), which was shown to be the best model for estimating both size fractions and fractionated Chl*a*, to satellite data to analyse the spatio-temporal variability of PSC within the SBB. For this, we used 8-day (1 km) composites of OLCI OC and MUR SST products within two seasonal periods sampled during the

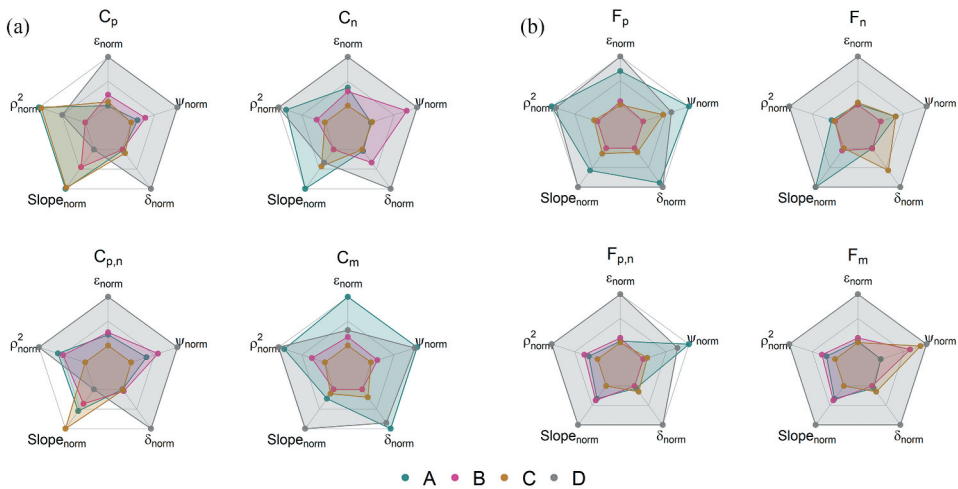


Figure 12. Radar charts for the size classes and models, satellite validation. With the performance metrics of each model (A–D) (a) for the fractionated Chla of each size class (C_p , C_n , and C_m) and (b) the correspondent fractions (F_p , F_n , and F_m) when compared with the *in situ* validation data.

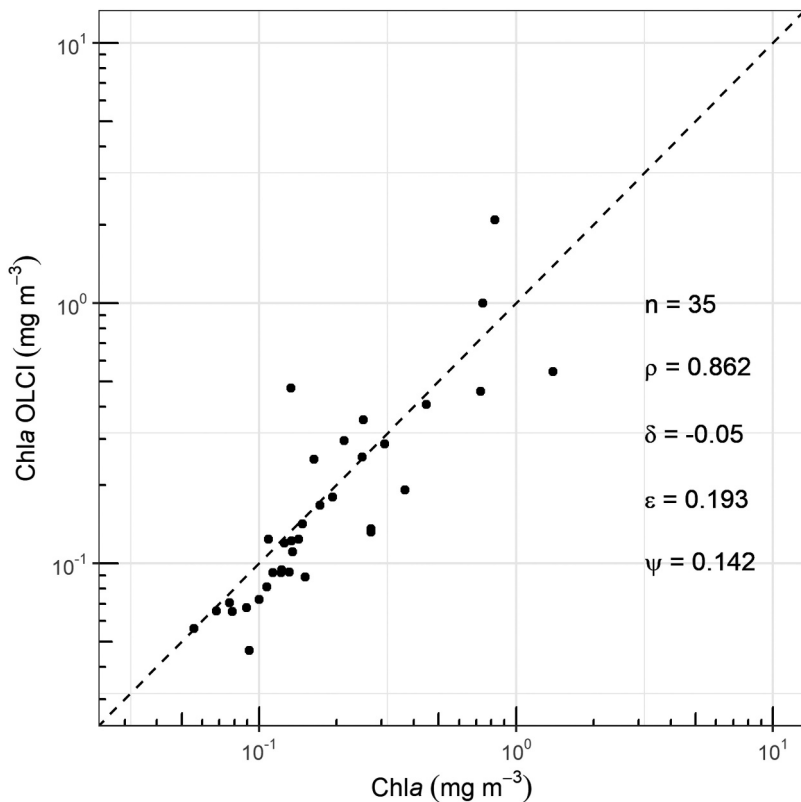


Figure 13. Validation of the total chlorophyll-*a* concentration estimated from the OLCI ocean colour product (OC4 and CI), by comparison with *in situ* data. Here, n is the number of observations, ρ is the correlation coefficient, δ is the bias, ϵ is the root mean square error, and ψ is the mean absolute error.

in situ survey – the austral winter (26 August 2019 to 1 September 2019) and summer (16 March 2022 to 22 March 2022). The 8-day Chla OLCI composite is shown in Figure 14(c,d) and the MUR SST composite in Figure 14(a,b). We see the marked difference in SST patterns in the two periods. During the winter, the SST is below 25°C and reaches low values around 15°C in the southern SBB shelf, off Santa Catarina (Figure 14(a)). In contrast, during the summer, temperatures are above 25°C for most of the area, except for the northern part near Cabo Frio (CF), associated with coastal upwelling, where temperatures are around 22°C (Figure 14(b)). The pattern observed for Chla is of higher phytoplankton biomass over the entire SBB, including waters beyond the shelf (> 200 m), in the winter (Figure 14(c)) compared with the same area in the summer (Figure 14(d)). Both periods showed high Chla near the coast, but in the winter these high values extended across the shelf, especially in the southern sector, which also showed lower SST.

The PSC model results captured the influence of the contrasting patterns of Chla and SST between winter and summer in the SBB. In the winter, the pico-size class (F_p) contributed less than 50% for most of the continental shelf, with a higher contribution in the oceanic domain (near 50%) (Figure 15(a)). In the summer, F_p contribution is about 75% in part of the shelf and in the offshore oceanic extension, and only the areas closer to the coast show contributions below 50% (Figure 15(b)).

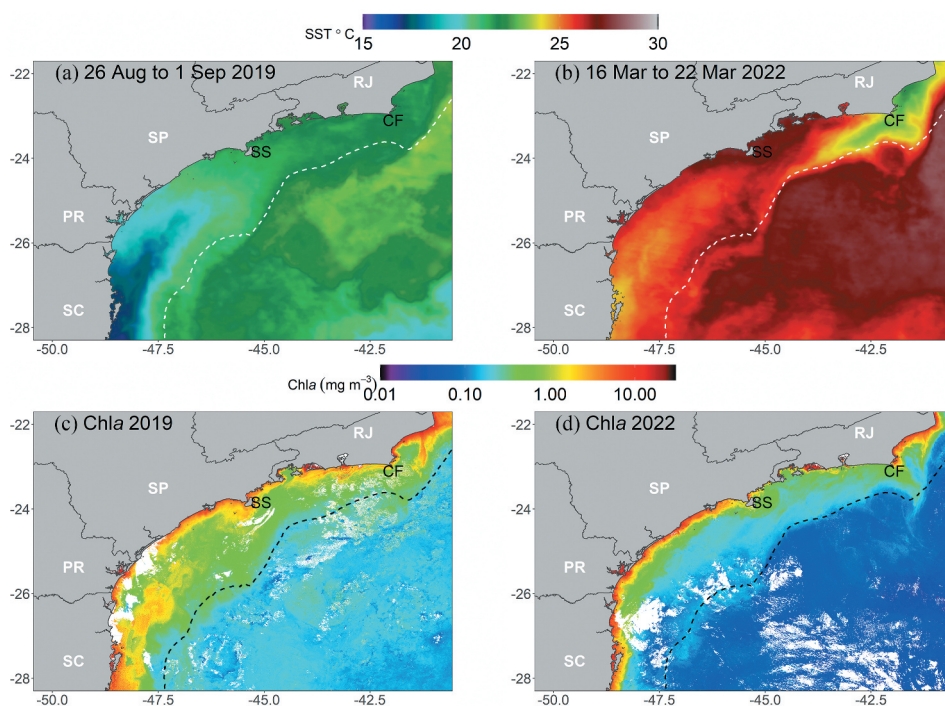


Figure 14. Mean conditions in two seasonal periods, 26th August 2019 to 1st September 2019 (a and c) and 16th March 2022 to 22nd March 2022 (b and d). A and B are the 8-day composite of the MUR SST. C and D are the composites of Chla from the sentinel 3A and 3B OLCI sensors. SS represents the São Sebastião Island, and CF represents Cabo Frio. The dashed line represents the 200 m isobath indicating the shelf break.

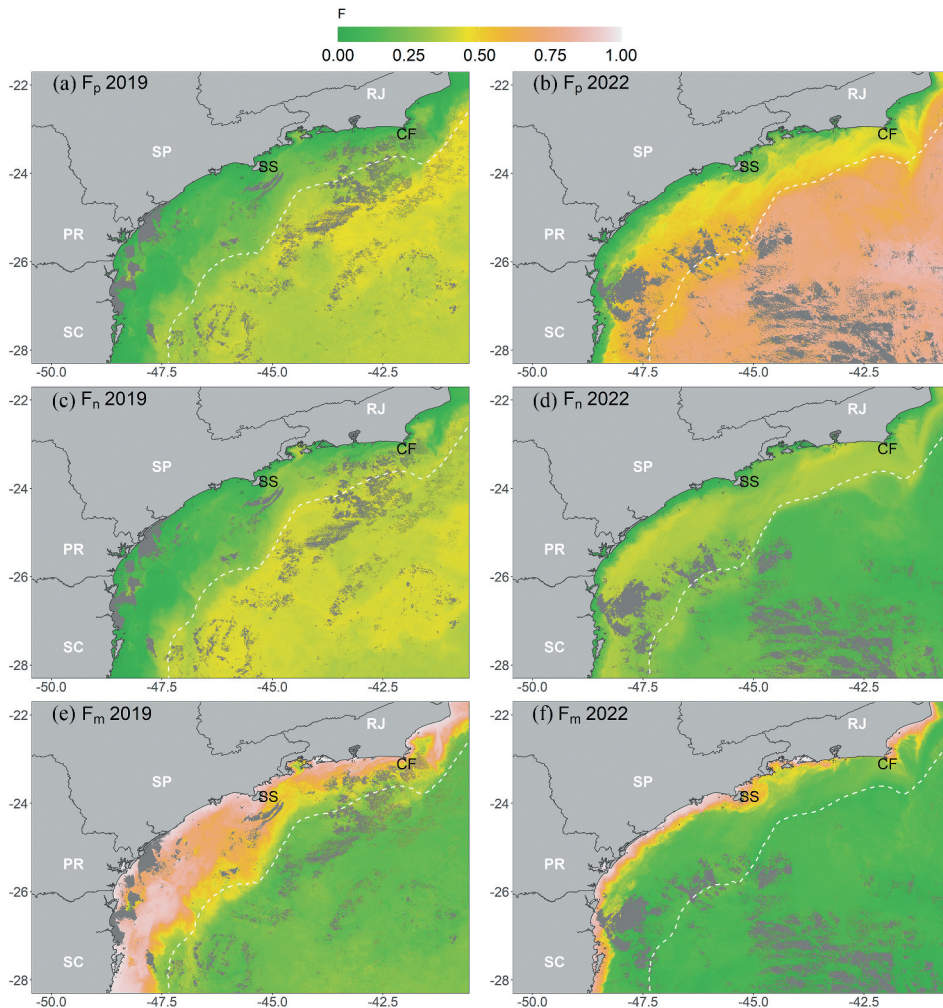


Figure 15. Results of the PSC model C, for the proportions of each size class considered. SS represents the São Sebastião Island, and CF represents Cabo Frio. The dashed white line is the 200 m isobath representing the shelf break. Images were derived from the sentinel 3A and 3B OLCI sensor and the MUR SST composite for these time periods. (a), (c) and (e) represent the results from 26th August 2019 to 1st September 2019. (b), (d) and (f) represent the results from 16th March 2022 to 22nd March 2022. (a) and (d) are the picoplankton fraction; (c) and (d) are the nanoplankton fraction. (e) and (f) are the microplankton fractions.

For the nano-size class (F_n), a higher contribution was observed in the oceanic domain (beyond the shelf break) in the winter (40–50%), compared with the shelf (< 30%) (Figure 15(c)). In the summer, an opposite pattern was observed with the highest contribution of this size class in the shelf domain, except for the region closer to the coastal interface (Figure 15(d)).

Micro-sized class dominated the shelf and coastal region in the winter, reaching proportions higher than 75% in some areas (Figure 15(e)), and decreased sharply in the oceanic domain. In the summer, important contributions of this size class were restricted

to areas under the influence of the coastal domain (Figure 15(f)), benefiting from the nutrients brought in by the continental runoff and coastal upwelling.

The spatial distribution for the size class fractions for the other models considered in this study are available in the Supplementary Material.

4. Discussion

The regional PSC SST-dependent Model C and the SST-threshold Model B for the South Brazil Bight gave better results than the SST-independent Model A and the global SST-dependent Model D models, even with a narrower SST range within the SBB, compared with the global SST-dependent models (Sun et al. 2023). It is worth considering some notable oceanographic features of the study area such as the seasonal cold water intrusion from the La Plata Plume Water during the winter and autumn (Piola et al. 2008), the greater influence of the warm and salty Tropical Water during the summer and spring, the coastal upwelling events of the South Atlantic Central Water (SACW) in Cabo Frio (Cerdeira and Castro 2014), and the spreading of estuarine waters across the inner shelf which is mainly restricted to the inner shelf during the summer (Brandini 2018). Of note is the observed SST median of about 23.8°C found in the *in situ* dataset, which was successfully used as a threshold for the model parameterisation (Model B). During the winter 2019 campaign, the observed maximum temperature was 24.55°C (min = 17.67°C, max = 24.55°C, mean = 21.68°C). During the spring and summer 2021–2022 campaign, the minimum temperature was 23.13°C (min = 23.13°C, max = 27.86°C, mean = 25.64°C). For each season, the relationship between the PSC community and TChl_a differs, and these variations are captured by the distinct model parameterisations.

The main difference in the SST threshold models is the higher temperature in the SBB region, 23.8°C compared to 15°C in Brewin et al. (2017). We see that for both above/below the threshold, the $C_{p,n}^{max}$ values were lower than those in the Brewin et al. (2017) model (see Table 2), probably due to the differences in the range of temperature involved, and indicating that the higher the temperature the lower the $C_{p,n}^{max}$. The C_p^{max} was also lower for the upper and lower thresholds compared to Brewin et al. (2017). Conversely, the $D_{p,n}$ and D_p were higher in the SBB compared with the values in Brewin et al. (2017), for both upper and lower thresholds.

Previous studies in the SBB suggested that this region hosts a more diverse and stable phytoplankton community (Brandini, Tura, and Santos 2018), whereas higher latitudes regions such as the Patagonian Shelf are characterised by a more productive but less diverse phytoplankton community (Fernandes and Brandini 1999; Olguin et al. 2006) driven by strong seasonal variability that enhances competition among phytoplankton species (de Oliveira Carvalho et al. 2022). However, Carvalho et al. (2022) based their findings on data collected during a single season (spring). Our results indicate that even the subtropical SBB is subject to marked seasonal variability in oceanographic conditions, which may affect the phytoplankton community in line with the patterns reported by Brandini, Tura, and Santos (2018).

In addition, including SST in the PSC model, rather than applying a seasonal division, provided more accurate estimates of PSC fractions during recurrent upwelling events

(both in coastal and shelf break waters) in the spring and summer. These events locally reduce SST, while nutrient intrusions stimulate phytoplankton growth. Although SST alone does not directly predict the dominance of micro-sized phytoplankton, it acts as a tracer of nutrient enrichment and favourable conditions for biomass accumulation (TChla), with greater contributions from micro-sized groups (F_m and C_m), as illustrated by the low-SST, high-Chla, high- F_m conditions near Cabo Frio (Figure 14 and 15). Therefore, an adjusted Chla-PSC relationship that accounts for lower vs. higher SST conditions can improve PSC estimates in complex systems influenced by coastal upwelling.

Considering the accuracy of the regional SST-dependent model, our results are consistent with the findings of Turner et al. (2021), who showed an improvement in accuracy of all size classes when SST dependence was included in the PSC estimation for the regional model in the Northeast U.S. continental shelf.

The PSC models failed only on a few occasions identified as possible outliers, with an absolute difference of any of the estimated fractionated Chla higher than 0.8. In the case of station D5 (shelf break sampled during the summer), the PSC models overestimated C_n and C_p , and underestimated the micro-size phytoplankton (C_m) (see Figure 7 c, g, k, o). The microscopic cell counts recorded a high microplankton biomass (98×10^3 cells L^{-1}) (Fernandes, Tremarin, and Faria 2022). Hence, the microplankton contribution was reasonably well estimated by the fucoxanthin and peridinin pigments which agreed well with the microscopic counting, and what also seems to be the case of the other size classes estimations by the DPA. The PSC model estimates average conditions based on the relationship between TChla, SST and PSCs. However, when these relationships deviate from the average, outliers may emerge. For this particular case, the diatom density was relatively high at the shelf break in the summer (Fernandes, Tremarin, and Faria 2022), while TChla and SST values were not particularly different from the average, nor was the nutrient concentration. Therefore, all model inputs indicated average conditions, but the actual PSC composition deviated from what was expected. Perhaps previous local upwelling induced by shelf break eddies (Palma and Matano 2009) may have triggered the higher concentration of microplankton at this location. This community could have been sustained even after apparent nutrient depletion, as linkages between physical and biological responses have different timings which are not always captured by statistical models. These are speculations that could be elucidated with further investigations using auxiliary data and highlight the complexities of coastal environments for PSC models.

For the other outliers, the contrary occurred, with the C_m overestimation by the PSC models. In the case of stations C7 and E7, sampled during the winter at deep waters, the microscopy analysis revealed a higher proportion of mixotrophic ciliates, followed by diatoms and coccolithophores in this oceanic portion of the study region (Fernandes, Tremarin, and Faria 2022). This possibly led to an underestimation of the micro-sized class by the DPA, since the mixotrophic ciliates may keep the plastids (and therefore the pigments) from nano-sized cells. The other two potential outliers, which also appeared to be overestimating the micro-sized cells by the PSC models, were from stations E2 and B3, located at inner/mid shelf waters and sampled during the summer. Despite the different conditions, the microscopy analysis also revealed a high contribution of mixotrophic

dinoflagellates and ciliates (Fernandes, Tremarin, and Faria 2022) (see Figure 7, B3 and E2 summer), which might also have caused this interference in the DPA estimations, i.e. overestimating the nano in the pigments estimations due to the plastids (biomarkers pigments), from smaller cells contained in larger cells. In these cases, the PSC models seem to be correct in relation to the micro-size classes, but not necessarily agreed to the phytoplankton groups that are usually associated to them by the DPA estimations, such as diatoms and dinoflagellates. Instead, ciliates and other mixotrophic species seem to be the most responsible for the micro-size contribution, as revealed by the microscopy analysis. The overall supposition is that, for these cases, the average SST and TChl a conditions indicated a higher contribution of micro-size classes, which were 'correctly' estimated by the PSC models, but the DPA used as reference were biased due to the presence of mixotrophic species.

Considering the highlighted cases, further investigation is required, in particular, the presence of mixotrophic species, which are common in the study region and pose a challenge to the use of the DPA method (Oliveira et al. 2021) as a ground truth reference for phytoplankton size classes. These species introduce uncertainties in the diagnostic pigments used to determine the actual phytoplankton size classes present. The occurrence of these species underscores the importance of using complementary techniques to quantify phytoplankton size fractions for satellite-based estimates, such as microscopy, biomolecular analyses for pico-sized groups, fractionated chlorophyll- a filtration, and flow cytometry, among others.

Moreover, the 'mixotrophic paradigm' underscores the necessity for a precise classification of mixotrophic protists, which are frequently categorized in a manner that is open to interpretation (Flynn et al. 2019). It is imperative for marine ecologists to further understand the ecophysiology and the role of mixotrophic groups in marine ecosystems, as this information is pivotal in evaluating the effects of climate change on marine phytoplankton assemblages (Flynn et al. 2019; Mitra et al. 2014), and ultimately, validating satellite modelling of marine communities.

5. Concluding remarks

The inclusion of SST in the abundance-based PSC regional model for a subtropical area influenced by different water masses and seasonal oceanographic processes showed a consistent improvement in the validation results compared with the SST-independent model and a global SST-dependent model. This reinforces the relevance of regionalized approaches, particularly for coastal environments. The results underscore the importance of SST in parameterising the size classes, even in regions with narrow ranges of SST, helping to capture nuances of local conditions. The CCA analysis also suggests that other variables may be relevant to PSC models, such as mixed-layer depth, local depth, and depth of chlorophyll- a maximum. Although beyond the scope of this study, the inclusion of these variables could be further explored in future studies, though none of these variables are routinely available at present at the same temporal and spatial scales as satellite data. Future studies should also focus on understanding the impact of mixotrophic organisms, which are commonly reported in the region and could lead to

misleading results on the size classification of phytoplankton using diagnostic pigments, as pigments normally associated with pico or nano-sized fraction could be incorporated into larger mixotrophic (or symbiotic) cells, leading to misinterpretation of the pigment data when it comes to assigning biomarker pigments to different size classes.

Acknowledgement

The authors acknowledge support from the Santos Basin Regional Environmental Characterization Project (PCR-BS) - coordinated by PETROBRAS, the Agência Nacional do Petróleo (ANP), and the Instituto Brasileiro de Meio Ambiente (IBAMA), for the dataset used for validation. The study was financed in part by the Coordenação de Aperfeiçoamento de Pessoal de Nível Superior - Brazil (CAPES) - Finance Code 001, Agência Espacial Brasileira (AEB) and Instituto Nacional de Pesquisas Espaciais (INPE). ALO was supported by FUSP (2017/00686-0) and UKRI-EP SRC (EP/T003820/1). FDC, SVR, DS, LF and FB acknowledge grants from FUSP (2017/00686-0). MK acknowledges grants from FAPESP (2021/04128-8) and FUSP (2017/00686-0). We are grateful to all the researchers and crew who dedicated their time and talent to the sampling cruises and data processing. We thank Dr. Luciano Felício Fernandes' team for the microscopy reports. We also thank the European Space Agency for providing OLCI chlorophyll-*a* concentrations and the JPL MUR MEaSUREs Project for the GHRSSST MUR global foundation for sea surface temperature data.

Disclosure statement

No potential conflict of interest was reported by the author(s).

Funding

The work was supported by the Fundação de Amparo à Pesquisa do Estado de São Paulo [2021/04128-8]; Fundação de Apoio à Universidade de São Paulo [2017/00686-0]; UKRI-EP SRC [EP/T003820/1].

ORCID

Andréa de Lima Oliveira  <http://orcid.org/0000-0002-2769-8168>
Natália Rudorff  <http://orcid.org/0000-0003-3451-4512>
Shubha Sathyendranath  <http://orcid.org/0000-0003-3586-192X>
Fabio Dall Cortivo  <http://orcid.org/0000-0003-3445-7490>
Silvana Vianna Rodrigues  <http://orcid.org/0000-0003-4394-7440>
Daniela Sudatti  <http://orcid.org/0000-0001-6057-2383>
Frederico Brandini  <http://orcid.org/0000-0002-3177-4274>
Milton Kampel  <http://orcid.org/0000-0002-0011-2083>

AI use statement

The authors did not use AI for generating text or figures in this paper.

Author contribution

ALO: Conceptualisation, Data Analysis, Methodology, Software, Validation, Writing – original draft, Writing – review and editing. NR: Conceptualisation, Methodology, Data Analysis, Writing – review and editing. SS: Conceptualisation, Methodology and Writing – review and editing. FC: Methodology, Validation, Software and Writing – review and editing. SVR: Methodology, Data curation and Writing – review and editing. DS: Methodology, Data curation and Writing – review and editing. LFF: Methodology and Writing – review and editing. FB: Project administration, Methodology and Writing – review and editing. MK: Conceptualisation, Funding acquisition, Methodology, Writing – review and editing.

Data availability statement

The data that support the findings of this study are available from the corresponding author, ALO, upon reasonable request.

References

- Aiken, J., Y. Pradhan, R. Barlow, S. Lavender, A. Poulton, P. Holligan, and N. Hardman-Mountford. 2009. "Phytoplankton Pigments and Functional Types in the Atlantic Ocean: A Decadal Assessment, 1995–2005." *Deep Research Part II Topical Studies Oceanography* 56 (15): 899–917. <https://doi.org/10.1016/j.dsr2.2008.09.017>.
- Alvain, S., C. Moulin, Y. Dandonneau, and F. M. Breon. 2005. "Remote Sensing of Phytoplankton Groups in Case 1 Waters from Global SeaWiFS Imagery." *Deep fulloutl* 52:1989–2004. <https://doi.org/10.1016/j.dsr.2005.06.015>.
- Alvain, S., C. Moulin, Y. Dandonneau, and H. Loisel. 2008. "Seasonal Distribution and Succession of Dominant Phytoplankton Groups in the Global Ocean: A Satellite View." *Global Biogeochemical Cycles* 22 (3): 1–15. <https://doi.org/10.1029/2007GB003154>.
- Alves Junior, N., P. M. Meirelles, E. de Oliveira Santos, B. Dutilh, G. G. Z. Silva, R. Paranhos, A. S. Cabral, et al. 2015. "Microbial Community Diversity and Physical–Chemical Features of the Southwestern Atlantic Ocean." *Archives of Microbiology* 197 (2): 165–179. <https://doi.org/10.1007/s00203-014-1035-6>.
- Artega, L., M. Pahlow, and A. Oschlies. 2014. "Global Patterns of Phytoplankton Nutrient and Light Colimitation Inferred from an Optimality-Based Model." *Global Biogeochemical Cycles* 28 (7): 648–661. <https://doi.org/10.1002/2013GB004668>.
- Behrenfeld, M. J., R. T. O'Malley, E. S. Boss, T. K. Westberry, J. R. Graff, K. H. Halsey, A. J. Milligan, D. A. Siegel, and M. B. Brown. 2016. "Revaluating Ocean Warming Impacts on Global Phytoplankton." *Nature Climate Change* 6 (3): 323–330. <https://doi.org/10.1038/nclimate2838>.
- Bergo, N. M., C. N. Signori, A. M. Amado, F. P. Brandini, and V. H. Pellizari. 2017. "The Partitioning of Carbon Biomass Among the Pico- and Nano-Plankton Community in the South Brazilian Bight During a Strong Summer Intrusion of South Atlantic Central Water." *Frontiers in Marine Science* 4:1–12. <https://doi.org/10.3389/fmars.2017.00238>.
- Brandini, F. P. 2018. Phytoplankton Assemblages of the Subtropical South West Atlantic: Composition and Dynamics in Relation to Physical and Chemical Processes.. *Plankton Ecology of the Southwestern Atlantic: From the Subtropical to the Subantarctic Realm*, In edited by M. S. Hoffmeyer, M. E. Sabatini, F. P. Brandini, D. L. Calliari, and N. H. Santinelli. Cham: Springer International Publishing 129–148. <https://doi.org/10.1007/978-3-319-77869-3>.
- Brandini, F. P., R. M. Lopes, K. S. Gutseit, H. L. Spach, and R. Sassi. 1997. *Planctonologia na Plataforma Continental do Brasil: Diagnose e Revisão Bibliográfica*. Brasília: IBAMA.
- Brandini, F. P., P. M. Tura, and P. P. G. M. Santos. 2018. "Ecosystem Responses to Biogeochemical Fronts in the South Brazil Bight." *Progress in Oceanography* 164:52–62. <https://doi.org/10.1016/j.pocean.2018.04.012>.

- Brewin, R. J. W., S. Ciavatta, S. Sathyendranath, T. Jackson, G. Tilstone, K. Curran, R. L. Airs, et al. 2017. "Uncertainty in Ocean-Color Estimates of Chlorophyll for Phytoplankton Groups." *Frontiers in Marine Science* 4. <https://doi.org/10.3389/fmars.2017.00104>.
- Brewin, R. J. W., E. Devred, S. Sathyendranath, S. J. Lavender, and N. J. Hardman-Mountford. 2011. "Model of Phytoplankton Absorption Based on Three Size Classes." *Applied Optics* 50 (22): 4535–4549. <https://doi.org/10.1364/AO.50.004535>.
- Brewin, R. J. W., S. Sathyendranath, T. Hirata, S. J. Lavender, R. M. Barciela, and N. J. Hardman-Mountford. 2010. "A Three-Component Model of Phytoplankton Size Class for the Atlantic Ocean." *Ecological Modelling* 221 (11): 1472–1483. <https://doi.org/10.1016/j.ecolmodel.2010.02.014>.
- Brewin, R. J. W., S. Sathyendranath, T. Jackson, R. Barlow, V. Brotas, R. Airs, and T. Lamont. 2015. "Influence of Light in the Mixed-Layer on the Parameters of a Three-Component Model of Phytoplankton Size Class." *Remote Sensing of Environment* 168:437–450. <https://doi.org/10.1016/j.rse.2015.07.004>.
- Campos, E. J. D., D. Velhote, and I. C. A. Silveira. 2000. "Shelf Break Upwelling Driven by Brazil Current Cyclonic Meanders." *Geophysical Research Letters* 27 (6): 751–754. <https://doi.org/10.1029/1999GL010502>.
- Castro, B., F. Brandini, A. Pires-Vanin, and L. Miranda. 2006. "Multidisciplinary Oceanographic Processes on the Western Atlantic Continental Shelf Between 4°N and 34°S." In *The Sea*, edited by A. R. Robinson and K. H. Brink, 259–293. Cambridge: Harvard University Press.
- Castro, B. M. 2014. "Summer/Winter Stratification Variability in the Central Part of the South Brazil Bight." *Continental Shelf Research* 89:15–23. <https://doi.org/10.1016/j.csr.2013.12.002>.
- Castro, B. M., and L. B. Miranda. 1998. "Physical Oceanography of the Western Atlantic Continental Shelf Located Between 4° N and 34° S." In *The Sea* (John Wiley & Sons), edited by A. R. Robinson and K. H. Brink (John Wiley & Sons), 209–251.
- Cerda, C., and B. M. Castro. 2014. "Hydrographic Climatology of South Brazil Bight Shelf Waters Between Sao Sebastiao (24°S) and Cabo Sao Tome (22°S)." *Continental Shelf Research* 89:5–14. <https://doi.org/10.1016/j.csr.2013.11.003>.
- Cetinić, I., C. S. Rousseaux, I. T. Carroll, A. P. Chase, S. J. Kramer, P. J. Werdell, D. A. Siegel, et al. 2024. "Phytoplankton Composition from Space: Requirements, Opportunities, and Challenges." *Remote Sensing of Environment* 302:113964. <https://doi.org/10.1016/j.rse.2023.113964>.
- Ciotti, A. M., and A. Bricaud. 2006. "Retrievals of a Size Parameter for Phytoplankton and Spectral Light Absorption by Colored Detrital Matter from Water-Leaving Radiances at SeaWiFS Channels in a Continental Shelf Region off Brazil." *Limnology and Oceanography: Methods* 4 (7): 237–253. <https://doi.org/10.4319/lom.2006.4.237>.
- de Castro Filho, B. M., A. F. Pereira, A. de Caroli, H. F. Neto, G. C. A. Paschoal, I. C. A. da Silveira, and C. C. Amor. 2015. "Correntes e Massas de água na Plataforma Continental." In *Meteorologia e Oceanografia*, edited by R. P. Martins and G. S. Grossmann-Matheson, 191–254. Elsevier. <https://doi.org/10.1016/B978-85-352-6208-7.50012-X>.
- de Lima Oliveira, A., N. Rudorff, S. Sathyendranath, F. D. Cortivo, S. V. Rodrigues, D. Sudatti, and M. Kampel. 2025. "Phytoplankton Size Structure in a Subtropical Area from Ocean Colour and Its Applications." *Journal Marine Systems* 248:104036. <https://doi.org/10.1016/j.jmarsys.2024.104036>.
- de Oliveira Carvalho, A. D. C., R. Kerr, V. M. Tavano, and C. R. B. Mendes. 2022. "The Southwestern South Atlantic Continental Shelf Biogeochemical Divide." *Biogeochemistry* 159 (2): 139–158. <https://doi.org/10.1007/s10533-022-00918-8>.
- Devred, E., S. Sathyendranath, V. Stuart, H. Maass, O. Ulloa, and T. Platt. 2006. "A Two-Component Model of Phytoplankton Absorption in the Open Ocean: Theory and Applications." *Journal of Geophysical Research Oceans* 111 (C3): 1–11. <https://doi.org/10.1029/2005JC002880>.
- Devred, E., S. Sathyendranath, V. Stuart, and T. Platt. 2011. "A Three Component Classification of Phytoplankton Absorption Spectra: Application to Ocean Color Data." *Remote Sensing of Environment* 115 (9): 2255–2266. <https://doi.org/10.1016/j.rse.2011.04.025>.
- Dutkiewicz, S., A. E. Hickman, O. Jahn, S. Henson, C. Beaulieu, and E. Monier. 2019. "Ocean Colour Signature of Climate Change." *Nature Communications* 10 (1). <https://doi.org/10.1038/s41467-019-08457-x>.

- Emílsson, I. 1961. "The Shelf and Coastal Waters off Southern Brazil *." *Boletim do Instituto Oceanográfico* 11 (2): 101–111. <https://doi.org/10.1590/S0373-55241961000100004>.
- Fernandes, L. F., and F. P. Brandini. 1999. "Comunidades microplanctônicas no Oceano Atlântico Sul Ocidental: biomassa e distribuição em novembro de 1992." *Revista Brasileira de Oceanografia* 47 (2): 189–205. <https://doi.org/10.1590/S1413-77391999000200007>.
- Fernandes, L. F., and F. P. Brandini. 2004. "Diatom Associations in Shelf Waters off Paraná State, Southern Brazil: Annual Variation in Relation to Environmental Factors." *Brazilian Journal of Oceanography* 52 (1): 19–34. <https://doi.org/10.1590/s1679-87592004000100003>.
- Fernandes, L. F., P. I. Tremarin, and D. M. Faria. 2022. "Diversidade, Distribuição e Abundância do Nano- e do Microplâncton da Bacia de Santos Frederico Brandini." In *Projeto de Caracterização Ambiental Marinha da Bacia de Santos PCR-BS: Sistema Pelágico*, 692. PETROBRAS. <https://comunicabaciadesantos.petrobras.com.br/projeto-de-caracterizacao-regional-da-bacia-de-santos-pcr-bs->.
- Flynn, K. J., A. Mitra, K. Anestis, A. A. Anschutz, A. Calbet, G. D. Ferreira, N. Gypens, et al. 2019. "Mixotrophic Protists and a New Paradigm for Marine Ecology: Where Does Plankton Research Go Now?" *Journal of Plankton Research* 41 (4): 375–391. <https://doi.org/10.1093/plankt/fbz026>.
- GEBCO Bathymetric Compilation Group 2024. 2024 The GEBCO_2024 Grid - a continuous terrain model of the global oceans and land.. NERC EDS *British Oceanographic Data Centre NOC*. <https://doi.org/10.5285/1c44ce99-0a0d-5f4f-e063-7086abc0ea0f>.
- Grasshoff, K., K. Kremling, and M. Ehrhardt. 1999. *Methods of Seawater Analysis* (Wiley). <https://doi.org/10.1002/9783527613984>.
- Groom, S. B., S. Sathyendranath, Y. Ban, S. Bernard, B. Brewin, V. Brotas, C. Brockmann, et al. 2019. "Satellite Ocean Colour: Current Status and Future Perspective." *Frontiers in Marine Science* 6. <https://doi.org/10.3389/fmars.2019.00485>.
- Hirata, T., J. Aiken, N. Hardman-Mountford, T. J. Smyth, and R. G. Barlow. 2008. "An Absorption Model to Determine Phytoplankton Size Classes from Satellite Ocean Colour." *Remote Sensing of Environment* 112 (6): 3153–3159. <https://doi.org/10.1016/j.rse.2008.03.011>.
- Hu, C., Z. Lee, and B. Franz. 2012. "Chlorophyll a Algorithms for Oligotrophic Oceans: A Novel Approach Based on Three-Band Reflectance Difference." *Journal of Geophysical Research Oceans* 117 (C1): 1–25. <https://doi.org/10.1029/2011JC007395>.
- Jeffrey, S. W. 1997. "Application of Pigment Methods to Oceanography." In *Phytoplankton Pigments in Oceanography: Guidelines to Modern Methods*, edited by S. W. Jeffrey, R. F. C. Mantoura, and S. W. Wright, 661. Paris: UNESCO. <https://doi.org/10.1017/s0025315400036389>.
- JPL MUR MEaSUREs Project. 2015 GHRST Level 4 MUR Global Foundation Sea Surface Temperature Analysis. *PO.DAAC, CA, USA* 4.1. <https://doi.org/10.5067/GHGM-4FJ04>.
- Kostadinov, T. S., D. A. Siegel, and S. Maritorena. 2010. "Global Variability of Phytoplankton Functional Types from Space: Assessment via the Particle Size Distribution." *Biogeosciences* 7:3239–3257. <https://doi.org/10.5194/bg-7-3239-2010>.
- Li, Z., L. Li, K. Song, and N. Cassar. 2013. "Estimation of Phytoplankton Size Fractions Based on Spectral Features of Remote Sensing Ocean Color Data." *Journal of Geophysical Research Oceans* 118 (3): 1445–1458. <https://doi.org/10.1002/jgrc.20137>.
- López-Urrutia, Á., and X. A. G. Morán. 2015. "Temperature Affects the Size-Structure of Phytoplankton Communities in the Ocean." *Limnology & Oceanography* 60 (3): 733–738. <https://doi.org/10.1002/lno.10049>.
- Mahiques, M. M., M. G. Tessler, A. Maria Ciotti, I. C. A. E. Da Silveira, S. H. D. M. Sousa, R. C. L. Figueira, C. C. G. Tassinari, V. V. Furtado, and R. F. Passos. 2004. "Hydrodynamically Driven Patterns of Recent Sedimentation in the Shelf and Upper Slope Off Southeast Brazil." *Continental Shelf Research* 24 (15): 1685–1697. <https://doi.org/10.1016/j.csr.2004.05.013>.
- Mannino, A., M. G. Novak, N. B. Nelson, M. Belz, F. Berthon, N. V. Blough. 2019. "Measurement Protocol of Absorption by Chromophoric Dissolved Organic Matter (CDOM) and Other Dissolved Materials." In *Inherent Optical Property Measurements and Protocols: Absorption Coefficient*, edited by A. Mannino and M. G. Novak, 1–77. Dartmouth, NS, Canada: IOCCG Ocean Optics and Biogeochemistry Protocols for Satellite Ocean Colour Sensor Validation.

- Marañón, E., P. Cermeño, M. Latasa, and R. D. Tadonlélé. 2012. "Temperature, Resources, and Phytoplankton Size Structure in the Ocean." *Limnology & Oceanography* 57 (5): 1266–1278. <https://doi.org/10.4319/lo.2012.57.5.1266>.
- Martiny, A. C., C. T. A. Pham, F. W. Primeau, J. A. Vrugt, J. K. Moore, S. A. Levin, and M. W. Lomas. 2013. "Strong Latitudinal Patterns in the Elemental Ratios of Marine Plankton and Organic Matter." *Nature Geoscience* 6 (4): 279–283. <https://doi.org/10.1038/ngeo1757>.
- Minnett, P. J., A. Alvera-Azcárate, T. M. Chin, G. K. Corlett, C. L. Gentemann, I. Karagali, X. Li, et al. 2019. "Half a Century of Satellite Remote Sensing of Sea-Surface Temperature." *Remote Sensing of Environment* 233:111366. <https://doi.org/10.1016/j.rse.2019.111366>.
- Miranda, L. B. 1982. "Análise de Massas de água da Plataforma Continental e da Região Oceânica Adjacente: Cabo de São Tomé (RJ) à Ilha de São Sebastião (SP) (Universidade de São Paulo)."
- Mitra, A., K. J. Flynn, J. M. Burkholder, T. Berge, A. Calbet, J. A. Raven, E. Granéli, et al. 2014. "The Role of Mixotrophic Protists in the Biological Carbon Pump." *Biogeosciences* 11 (4): 995–1005. <https://doi.org/10.5194/bg-11-995-2014>.
- Möller, O. O., A. R. Piola, A. C. Freitas, and E. J. D. Campos. 2008. "The Effects of River Discharge and Seasonal Winds on the Shelf off Southeastern South America." *Continental Shelf Research* 28 (13): 1607–1624. <https://doi.org/10.1016/j.csr.2008.03.012>.
- Moreira, D. L., A. G. Dalto, A. G. Figueiredo Jr., A. M. Valerio, A. M. S. Detoni, A. C. T. Bonecker, C. N. Signori, et al. 2023. "Multidisciplinary Scientific Cruises for Environmental Characterization in the Santos Basin – Methods and Sampling Design." *Ocean and Coastal Research* 71 (suppl 3): 1–20. <https://doi.org/10.1590/2675-2824071.22072dlm>.
- Olguin, H. F., D. Boltovskoy, C. B. Lange, and F. Brandini. 2006. "Distribution of Spring Phytoplankton (Mainly Diatoms) in the Upper 50 M of the Southwestern Atlantic Ocean (30–61° S)." *Journal of Plankton Research* 28 (12): 1107–1128. <https://doi.org/10.1093/plankt/fbl045>.
- Oliveira, A. L., N. Rudorff, M. Kampel, S. Sathyendranath, M. Pompeu, A. M. S. Detoni, and G. M. Cesar. 2021. "Phytoplankton Assemblages and Optical Properties in a Coastal Region of the South Brazil Bight." *Continental Shelf Research* 227:104509. <https://doi.org/10.1016/j.csr.2021.104509>.
- O'Reilly, J. E., and P. J. Werdell. 2019. "Chlorophyll Algorithms for Ocean Color Sensors - OC4, OC5 & OC6." *Remote Sensing of Environment* 229:32–47. <https://doi.org/10.1016/j.rse.2019.04.021>.
- Palma, E. D., and R. P. Matano. 2009. "Disentangling the Upwelling Mechanisms of the South Brazil Bight." *Continental Shelf Research* 29 (11–12): 1525–1534. <https://doi.org/10.1016/j.csr.2009.04.002>.
- Piola, A. R., E. J. D. Campos, O. O. Möller, M. Charo, and C. Martinez. 2000. "Subtropical Shelf Front off Eastern South America." *Journal of Geophysical Research Oceans* 105 (C3): 6565–6578. <https://doi.org/10.1029/1999jc000300>.
- Piola, A. R., O. O. Möller, R. A. Guerrero, and E. J. D. Campos. 2008. "Variability of the Subtropical Shelf Front off Eastern South America: Winter 2003 and summer 2004." *Continental Shelf Research* 28 (13): 1639–1648. <https://doi.org/10.1016/j.csr.2008.03.013>.
- Ribeiro, C. G., A. L. dos Santos, D. Marie, V. H. Pellizari, F. P. Brandini, and D. Vaultot. 2016. "Pico and Nanoplankton Abundance and Carbon Stocks Along the Brazilian Bight." *PeerJ* 2016, 1–20. <https://doi.org/10.7717/peerj.2587>.
- Sanz, N., A. García-Blanco, P. Loures, and J. L. Garrido. 2015. "Phytoplankton Pigment Biomarkers: HPLC Separation Using a Pentafluorophenyl octadecyl Silica Column." *Methods Ecol. Evol.* 6: 1199–1209. [10.1111/2041-210X.12406](https://doi.org/10.1111/2041-210X.12406).
- Silveira, I. C. A., P. S. Bernardo, C. Z. Lazaneo, J. P. M. Amorim, M. Borges-Silva, R. C. Martins, D. M. C. Santos, et al. 2023. "Oceanographic Conditions of the Continental Slope and Deep Waters in Santos Basin: The SANSED Cruise (winter 2019)." *Ocean and Coastal Research* 71 (suppl 3). <https://doi.org/10.1590/2675-2824071.2206icas>.
- Silveira, I. C. A. D., A. C. K. Schmidt, E. J. D. Campos, S. S. D. Godoi, and Y. Ikeda. 2000. "A Corrente do Brasil ao Largo da Costa Leste Brasileira." *Revista Brasileira de Oceanografia* 48 (2): 171–183. <http://www.scielo.br/pdf/bjoe/v48n2/08.pdf>.
- Stock, A., and A. Subramaniam. 2020. "Accuracy of Empirical Satellite Algorithms for Mapping Phytoplankton Diagnostic Pigments in the Open Ocean: A Supervised Learning Perspective." *Frontiers in Marine Science* 7. <https://doi.org/10.3389/fmars.2020.00599>.

- Sun, X., R. J. W. Brewin, S. Sathyendranath, G. Dall, D. Antoine, R. Barlow, A. Bracher, et al. 2025. "Coupling Ecological Concepts with an Ocean-Colour Model: Parameterisation and Forward Modelling." *Remote Sensing of Environment* 316:114487. <https://doi.org/10.1016/j.rse.2024.114487>.
- Sun, X., R. J. W. Brewin, S. Sathyendranath, G. Dall'olmo, R. Airs, R. Barlow, A. Bracher, et al. 2023. "Coupling Ecological Concepts with an Ocean-Colour Model: Phytoplankton Size Structure." *Remote Sensing of Environment* 285:113415. <https://doi.org/10.1016/j.rse.2022.113415>.
- Tassan, S. 2002. "A Sensitivity Analysis of the "Transmittance-Reflectance" Method for Measuring Light Absorption by Aquatic Particles." *Journal of Plankton Research* 24 (8): 757–774. <https://doi.org/10.1093/plankt/24.8.757>.
- Tassan, S., and G. Ferrari. 1995. "An Alternative Approach to Absorption Measurements of Aquatic Particles Retained on Filters." *Limnology & Oceanography* 40 (8): 1358–1368. <https://doi.org/10.4319/lo.1995.40.8.1358>.
- Tenenbaum, D. R., M. C. Villac, S. C. Viana, M. Matos, M. Hatherly, I. V. Lima. 2004. *Phytoplankton Atlas of Sepetiba Bay, Rio de Janeiro, Brazil*. Rio de Janeiro/London: Global Ballast Water Management Programme <https://www.wcdn.imo.org/localresources/en/OurWork/PartnershipsProjects/Documents/Mono16.pdf>.
- Ter Braak, C. J. F., and P. F. M. Verdonschot. 1995. "Canonical Correspondence Analysis and Related Multivariate Methods in Aquatic Ecology." *Aquatic Sciences* 57 (3): 255–289. <https://doi.org/10.1007/BF00877430>.
- Turner, K. J., C. B. Mouw, K. J. W. Hyde, R. Morse, and A. B. Ciochetto. 2021. "Optimization and Assessment of Phytoplankton Size Class Algorithms for Ocean Color Data on the Northeast U.S. Continental Shelf." *Remote Sensing of Environment* 267:112729. <https://doi.org/10.1016/j.rse.2021.112729>.
- Uitz, J., H. Claustre, A. Morel, and S. B. Hooker. 2006. "Vertical Distribution of Phytoplankton Communities in Open Ocean: An Assessment Based on Surface Chlorophyll." *Journal of Geophysical Research Oceans* 111 (C8). <https://doi.org/10.1029/2005JC003207>.
- Valentin, J. L., D. L. Andre, and S. A. Jacob. 1987. "Hydrobiology in the Cabo Frio (Brazil) Upwelling: Two-Dimensional Structure and Variability During a Wind Cycle." *Continental Shelf Research* 7 (1): 77–88. [https://doi.org/10.1016/0278-4343\(87\)90065-3](https://doi.org/10.1016/0278-4343(87)90065-3).
- Villac, M. C., V. A. D. P. Cabral-Noronha, and T. D. O. Pinto. 2008. "The Phytoplankton Biodiversity of the Coast of the State of São Paulo, Brazil." *Biota Neotropica* 8 (3): 151–173. <https://doi.org/10.1590/S1676-06032008000300015>.
- Werdell, J., J. O'Reilly, C. Hu, L. Feng, Z. Lee, B. Franz. 2023. "Chlorophyll A V.1.1." <https://doi.org/10.5067/JCQB8QALDOYD>.
- Werdell, P. J., and S. W. Bailey. 2005. "An Improved In-Situ Bio-Optical Data Set for Ocean Color Algorithm Development and Satellite Data Product Validation." *Remote Sensing of Environment* 98 (1): 122–140. <https://doi.org/10.1016/j.rse.2005.07.001>.

Appendix A

Table A1. Definitions of the abbreviations and symbols used in this manuscript.

Abbreviation and Symbol	Definition	Unit
CCA	Canonical Correspondence Analysis	
CDOM	coloured dissolved organic matter	
Chla	Chlorophyll-a concentration	mg m ⁻³
CW	Coastal Water	
DPA	diagnostic pigment analysis	
GHRSTT	Group for High Resolution Sea Surface Temperature	
HPLC	High Performance Liquid Chromatography	
MUR	Multi-scale Ultra-high Resolution	
PACE	Plankton, Aerosol, Cloud, ocean Ecosystem	
PSCs	Phytoplankton Size Classes	
PPW	Plata Plume Water	
OCI	Ocean Colour Instrument	
OLCI	Ocean and Land Colour Instrument	
SBB	South Brazil Bight	
SACW	South Atlantic Central Water	
SSF	Subtropical Shelf Front	
SST	sea surface temperature	°C
TChla	is the sum of the following pigments monovinyl chlorophyll-a, divinyl-chlorophyll-a, chlorophyllide-a, chlorophyll-a allomers and epimers, in this study this is the in situ chlorophyll-a concentration.	mg m ⁻³
TW	Tropical Water	
C_w	weighted sum of the seven diagnostic pigments	mg m ⁻³
$C_{pr}, C_{nr}, C_{mr}, C_{p,n}$	Concentration of picoplankton, nanoplankton, microplankton, and combined pico- and nanoplankton	mg m ⁻³
$C_{p,n}^{max}, C_p^{max}$	Asymptotic maximum values for combined pico- and nanoplankton and picoplankton	mg m ⁻³
$D_p, D_{p,n}$	Fraction of Chla as total Chla tends to zero for combined pico- and nanoplankton and picoplankton	dimensionless
$F_{pr}, F_{nr}, F_{mr}, F_{p,n}$	Fraction of picoplankton, nanoplankton, microplankton, and combined pico- and nanoplankton	dimensionless
J_a, J_b, J_c, J_d	Parameters for $D_{p,n}$ in Global SST-dependent	dimensionless, °C ⁻¹ , °C, dimensionless
K_a, K_b, K_c, K_d	Parameters for $C_{p,n}^{max}$ in Model C, K_a is the height of peak, K_b is the positions of peak centre, and K_c controls the width of the curve, and K_d is the lower limit for $C_{p,n}^{max}$.	mg m ⁻³ , °C ⁻¹ , °C, mg m ⁻³
L_a, L_b, L_c, L_d	Parameters for C_p^{max} in Model C, same as K_a to K_d	mg m ⁻³ , °C ⁻¹ , °C, mg m ⁻³ , mg m ⁻³
M_a, M_b, M_c	Parameters for $D_{p,n}$ in Model C, same as K_a to K_c	mg m ⁻³ , °C ⁻¹ , °C, mg m ⁻³³
O_a, O_b, O_c, O_d	Parameters for $D_{p,n}$ in Global SST-dependent (Model A) and in the regional SST-dependent (Model C)	dimensionless, °C ⁻¹ , °C, dimensionless
U_a, U_b, U_c	Parameters for $C_{p,n}^{max}$ in Global SST-dependent model	mg m ⁻³ , °C ⁻² , mg m ⁻³ , °C ⁻¹ , mg m ⁻³ mg
$V_a, V_b, V_c, V_d, V_e, V_f$	Parameters for C_p^{max} in Global SST-dependent model, V_a and V_d are the height of peaks, V_b and V_c are the positions of peak centres, and V_e and V_f control the width of the curve	mg m ⁻³ , °C, °C, mg m ⁻³ , °C, °C
W	Weights of pigments in diagnostic pigment analyse	dimensionless
δ	bias	dimensionless
ϵ	RMSE root mean square error	dimensionless
ψ	MAE mean absolute error	dimensionless
ρ	correlation coefficient	dimensionless
δ_{norm}	Normalised bias	dimensionless
ϵ_{norm}	Normalised RMSE	dimensionless
ψ_{norm}	Normalised MAE	dimensionless
$Slope_{norm}$	Normalised slope	dimensionless
ρ_{norm}^2	Normalised determination coefficient	dimensionless